photonics

MDPI

Article

Fundamental Studies on Electron Dynamics in Exact Paraxial Beams with Angular Momentum

Ignacio Pastor [1,*], Ramón F. Álvarez-Estrada [2], Luis Roso [3] and Francisco Castejón [1]

[1] Laboratorio Nacional de Fusión, CIEMAT, Avenida Complutense 40, E-28040 Madrid, Spain; francisco.castejon@ciemat.es
[2] Departamento de Física Teórica, Facultad de Ciencias Físicas, Universidad Complutense, E-28040 Madrid, Spain; rfa@ucm.es
[3] Centro de Láseres Pulsados, CLPU, Scientific Park, Villamayor, E-37185 Salamanca, Spain; roso@clpu.es
* Correspondence: ignacio.pastor@ciemat.es

Abstract: Classical electromagnetic radiation with orbital angular momentum (OAM), described by nonvanishing vector and scalar potentials (namely, Lorentz gauge) and under Lorentz condition, is considered. They are employed to describe paraxial laser beams, thereby including non-vanishing longitudinal components of electric and magnetic fields. The relevance of the latter on electron dynamics is investigated in the reported numerical experiments. The lowest corrections to the paraxial approximation appear to have a negligeable influence in the regimes treated here. Incoherent Thomson scattering (TS) from a sample of free electrons moving subject to the paraxial fields is studied and investigated as a beam diagnosis tool. Numerical computations elucidate the nature and conditions for the so called trapped solutions (electron motions bounded in the transverse plane of the laser and drifting along the propagation direction) in long quasi-steady laser beams. The influence of laser parameters, in particular, the laser beam size and the non-vanishing longitudinal field components, essential for the paraxial approximation to hold, are studied. When the initial conditions of the electrons are sufficiently close to the origin, a simplified model Hamiltonian to the full relativistic one is introduced. It yields results comparing quite well quantitatively with the observed amplitudes, phase relationships and frequencies of oscillation of trapped solutions (at least for wide laser beam sizes). Genuine pulsed paraxial fields with OAM and their features, modeling true ultra-short pulses are also studied for two cases, one of wide laser beam spot (100 μm) and other with narrow beam size of 6.4 μm. To this regard, the asymptotic distribution of the kinetic energy of the electrons as a function of their initial position over the transverse section is analyzed. The relative importance of the transverse structure effects and the role of longitudinal fields is addressed. By including the full paraxial fields, the asymptotic distribution of kinetic energy of an electron population distributed across the laser beam section, has a nontrivial and unexpected rotational symmetry along the optical propagation axis.

Keywords: lorentz gauge and condition; orbital angular momentum beams; paraxial approximation and corrections; electron dynamics in full paraxial fields; nonlinear thomson scattering

Citation: Pastor, I.; Álvarez-Estrada, R.F.; Roso, L.; Castejón, F. Fundamental Studies on Electron Dynamics in Exact Paraxial Beams with Angular Momentum. *Photonics* **2022**, *9*, 693. https://doi.org/10.3390/photonics9100693

Received: 2 August 2022
Accepted: 16 September 2022
Published: 26 September 2022

1. Introduction

Ultra intense pulsed lasers, available nowadays in the near infrared range, have reached peak powers in the multi-petawatt domain [1]. When tightly focused they allow extraordinary intensities, or in other words extraordinary concentrations of energy. Today's record is the 10^{23} W/cm^2, that has been achieved in the Korean multi petawatt laser [2]. Neutral atoms do not survive such enormous intensities. First ionization occurs by the mechanism of above threshold ionization well before 10^{17} W/cm^2 for most atoms and, arriving to 10^{18} W/cm^2, the only thing we have are relativistic electrons and positive ions (singly or multiply charged). Observe that all occurs during the turn on of the pulse. Such

lasers have durations of a few tens of femtoseconds for the so-called intensity lasers (as the Korean one) to picoseconds for the so-called energy lasers.

Positive ions move obviously much slower than electrons due to the different mass/charge ratio. Then, the accelerated electrons released from those atoms become highly relativistic as laser intensities increase towards 10^{23} W/cm^2. The intensities considered in the present work will lie well above 10^{18} W/cm^2, so that electrons will be certainly relativistic, yet without reaching 10^{23} W/cm^2. Moreover, at such record peak intensities, radiation reaction [3] may start to play a role on the electron dynamics: then, we shall not be concerned with radiation reaction in the present work.

The scattering of electromagnetic radiation (Thomson Scattering, denoted hereafter by TS) by free charges provides a very interesting diagnostic. In fusion plasmas, TS yields electron distribution functions and, hence, their density distributions (see for example [4,5]). TS is also potentially useful and challenging for the diagnosis of intense or ultra-intense laser beams. In fact, as discussed above, the acceleration of the electrons is the dominant process for light scattering: electrons driven by the pulse laser move relativistically and radiate due to TS. The diagnoses in both cases are obtained from the analysis of the detected scattered radiation (spectrum, polarization, etc.).

A large part of the present work will be concerned with laser beams with orbital angular momentum (OAM). For different complementary studies about them, see for example [6–9] and also [10–15] for some experiments with light and theoretical work altogether, in states having OAM. Those beams have remarkable properties even if their structure is quite different from the ordinary plane wave ones. For example, selection rules for the photoelectric effect with OAM photons hold provided that the photon orbital angular momentum be included in the former [16]. Moreover recent experiments succeeded in getting high intensity OAM modes using off-axis spiral phase mirrors [17].

In modern petawatt laser sources it seems possible and quite appealing to include a variety of transverse structures (for instance, a general Laguerre-Gauss mode, with a step function to account for its time pulsed structure). Such structures may influence strongly the laser-atom or laser-electron interaction. Even if to achieve such OAM pulses at multi-joule level is difficult, it seems very reasonable to investigate various possible physical processes generated by them: the motion of a fully relativistic electron subject to OAM pulses is a particularly appealing case.

On the other hand, transverse pulsed plane wave beams turn out to be very useful, not only by themselves but, in particular, as possible approximations of other beams in some restricted ranges, under certain conditions. Thus, with the second purpose in mind, a comparatively small part of our study (Appendix A and Section 4) will consider transverse pulsed plane wave beams as approximations to OAM ones.

Plane wave models, or pulsed plane waves, cannot account for the total finite energy content of electromagnetic fields of current ultra-intense lasers. There is much current interest in studying ultra-intense laser fields with models beyond the simple plane wave approximation. For that purpose, paraxial fields that include the transverse structure of laser fields have been intensively studied, in particular a family of modes which have a net OAM. For interesting studies about the paraxial approximation to describe electromagnetic waves see, for instance, [18–20] and references therein.

It is well known that in order to fulfill the paraxial approximation the laser fields have to acquire non-vanishing longitudinal components of the electric and magnetic field, and one of the goals of this paper is to clarify their relevance on electron dynamics in well controlled numerical experiments. We remind that the longitudinal E_z and B_z components have an influence which scales with the inverse of the laser beam size.

In [21], we have studied the dynamics and TS of electrons subject to ultra intense laser radiations with OAM beams, mostly numerically. In [22], the analysis, combining analytical and numerical procedures, treated laser radiations represented by either plane waves with general elliptic polarization or simpler OAM beams with vanishing longitudinal components of the electric and magnetic field, and analyzed possible approximations

to such OAM beams by means of plane waves, in certain regimes. The present work will extend non-trivially [22] to ultra intense laser beams with OAM and non-vanishing longitudinal components of the electric and magnetic fields. Our approach here to the paraxial approximation and eventual corrections thereof will be based on vector and scalar potentials in Lorentz gauge and under Lorentz condition.

Numerical computations will be carried out in order to compare our paraxial approach with the one by Erikson and Singh [18]. To our knowledge this model represents a very useful compromise between the complexity of a full vectorial description of the laser field and the oversimplification of using only the the transverse part of the field. Erikson and Singh's model is a reasonable description of the focus of the laser beam or a laser pulse provided that the f# (the ratio of the focal length of a mirror or lens to its diameter) is not too short (in other words, provided that the paraxial approximation holds). As an approximate criterion we can say that this works for long focus, f#/10 or longer. In the case of very tight focus, as the f#/1.1 of [2] a more complete description of the counter propagating components is desirable. The model we present is, to our knowledge, a new way to introduce the longitudinal components to increase accuracy in the description without increasing the complexity of the model.

We discuss the TS emission from free electrons interacting with paraxial fields, and evaluate its diagnostic capabilities to ascertain averaged or statistical properties of the electron samples and of the beam under study.

Section 2 reminds the Maxwell equations in Lorentz gauge, with Lorentz condition and formulates exact equations for modulated plane-waves, which will provide the basis for the present study of the paraxial approximation and corrections thereof. Section 2 also discusses the paraxial approximation in the present framework. Section 3 analyzes trapped electron trajectories in long quasi-steady laber beams with OAM. Section 4 is devoted to ultrashort-pulse paraxial laser beams with OAM. Section 4 also deals with numerical computations for the solution for a pulsed plane wave with Gaussian envelope, given in Appendix A. Appendix A will treat analytical solutions of the electron dynamics in a pulsed plane wave with Gaussian envelope. A novel approach to corrections to the paraxial approximation is included in Appendix B.

2. General Aspects

2.1. Maxwell Equations in Lorentz Gauge

The Maxwell equations for electric (**E**) and magnetic (**B**) fields in vacuum and in the absence of charges read (in SI units) [23]:

$$\begin{aligned} \nabla_{\mathbf{x}} \cdot \mathbf{E} = 0, \frac{\partial \mathbf{B}}{\partial t} = -\nabla_{\mathbf{x}} \times \mathbf{E} \\ \nabla_{\mathbf{x}} \cdot \mathbf{B} = 0, \frac{1}{c^2} \frac{\partial \mathbf{E}}{\partial t} = \nabla_{\mathbf{x}} \times \mathbf{B} \end{aligned} \tag{1}$$

c being the velocity of light in vacuum. They all depend on the three-dimensional position $\mathbf{x} = (x, y, z) = (\bar{x}, z)$ and on time t. Let $\mathbf{A}$ and Φ be the vector and scalar potentials. The Lorentz gauge will be employed and the Lorentz condition reads:

$$\frac{1}{c^2} \frac{\partial \Phi}{\partial t} + \nabla_{\mathbf{x}} \cdot \mathbf{A} = 0 \tag{2}$$

In this gauge, the fields are:

$$\mathbf{E} = -\frac{\partial \mathbf{A}}{\partial t} - \nabla_{\mathbf{x}} \Phi, \mathbf{B} = \nabla_{\mathbf{x}} \times \mathbf{A}. \tag{3}$$

The wave equations for the potentials read:

$$\frac{1}{c^2} \frac{\partial^2 \mathbf{A}}{\partial t^2} = \nabla_{\mathbf{x}}^2 \mathbf{A}, \frac{1}{c^2} \frac{\partial^2 \Phi}{\partial t^2} = \nabla_{\mathbf{x}}^2 \Phi \tag{4}$$

For convenience, the fields and the potentials will be supposed to be complex (the physical fields and potentials being their real parts).

2.2. Exact Modulated Plane-Wave Equations

Exact solutions of Equation (4) and hence, of the Maxwell equations, will be searched with the structure of modulated plane-waves traveling along the z-axis with wavevector k_0 and frequency ω_0 ($\omega_0 = ck_0$). These solutions are particularly well adapted to model very long laser pulses, where their precise temporal envelope can be disregarded. They read:

$$X = X_{ex}(\bar{x}, z) \exp i(k_0 z - \omega_0 t + \chi_0) \tag{5}$$

for $X = \Phi, A, E, B$. The exact equations fulfilled by all $X_{ex}(\bar{x}, z)$ will be given below. Let: $\nabla_{\mathbf{x}} = (\nabla_{\bar{x}}, \partial/\partial z)$, $X = (\bar{X}, X_z)$ for the various X. One finds:

$$\left(\nabla_{\bar{x}}^2 + \frac{\partial^2}{\partial z^2} + 2ik_0 \frac{\partial}{\partial z}\right) X_{ex} = 0 \tag{6}$$

for $X_{ex} = \Phi_{ex}, \bar{A}_{ex}, A_{z,ex}$ and

$$\nabla_{\bar{x}} \bar{A}_{ex} + \frac{\partial}{\partial z} A_{z,ex} + ik_0 A_{z,ex} = \frac{i\omega_0}{c^2} \Phi_{ex} \tag{7}$$

For the electric and magnetic fields, one gets:

$$\bar{E}_{ex} = -\nabla_{\bar{x}} \Phi_{ex} + i\omega_0 \bar{A}_{ex} \tag{8}$$

$$E_{z,ex} = -ik_0 \Phi_{ex} - \frac{\partial}{\partial z} \Phi_{ex} + i\omega_0 A_{z,ex} \tag{9}$$

$$B_{x,ex} = \frac{\partial}{\partial y} A_{z,ex} - \left(ik_0 + \frac{\partial}{\partial z}\right) A_{y,ex} \tag{10}$$

$$B_{y,ex} = -\frac{\partial}{\partial x} A_{z,ex} + \left(ik_0 + \frac{\partial}{\partial z}\right) A_{x,ex} \tag{11}$$

$$B_{z,ex} = \frac{\partial}{\partial x} A_{y,ex} - \frac{\partial}{\partial y} A_{x,ex} \tag{12}$$

Without loss of generality, we shall choose:

$$A_{z,ex} = 0 \tag{13}$$

Then, for exact modulated plane-wave solutions, the knowledge of the two independent components $A_{x,ex}$ and $A_{y,ex}$ of $\bar{A}_{ex}$ just determines Φ_{ex}, $\mathbf{E}_{ex}$ and $\mathbf{B}_{ex}$. In particular, , one can develop successive approximations for $A_{x,ex}$ and $A_{y,ex}$, (independently of each other): the paraxial approximation (next section) and eventual extensions thereof (Appendix B).

2.3. General Paraxial Approximation

In general, the paraxial approximation $X_{ex} \simeq X_{par}$ for $X_{ex} = \Phi_{ex}, \bar{A}_{ex}, A_{z,ex}$ is based, in the present framework, upon assuming that $\frac{\partial^2}{\partial z^2} X_{ex}$ can be neglected compared to $(2k_0 \frac{\partial}{\partial z}) X_{ex}$. We shall disregard $A_{z,ex}$ completely, since we have chosen $A_{z,ex} = 0$ exactly from the outset (prior to imposing the paraxial approximation). Equation (6) yields:

$$\left(\nabla_{\bar{x}}^2 + 2ik_0 \frac{\partial}{\partial z}\right) X_{par} = 0 \tag{14}$$

Consequently, the latter determine directly Φ_{par} and the components of $\mathbf{E}_{par}$ and $\mathbf{B}_{par}$ (all of which, on the other hand, also fulfill Equation (14)). One has:

$$\nabla_{\bar{x}} \bar{A}_{par} = \frac{i\omega_0}{c^2} \Phi_{par} \tag{15}$$

In the work by Erikson and Singh [18], their lowest paraxial approximation is given by two independent functions f and g. A comparison with [18] shows that $i\omega_0 A_{x,par} = f$ and $i\omega_0 A_{y,par} = g$. It is stressed that the functions f and g in [18] (carrying no subscripts) should NOT be confused with the functions $g_{m,n}$ and $f_{m,n}$ (including subscripts) to be employed throughout the present paper (since the next subsection onwards). For the electric and magnetic fields, one gets:

$$\bar{E}_{par} = i\omega_0 \bar{A}_{par} \tag{16}$$

$$E_{z,par} = -ik_0 \Phi_{par} \tag{17}$$

$$B_{x,par} = -ik_0 A_{y,par} \tag{18}$$

$$B_{y,par} = ik_0 A_{x,par} \tag{19}$$

$$B_{z,par} = \frac{\partial}{\partial x} A_{y,par} - \frac{\partial}{\partial y} A_{x,par} \tag{20}$$

Equations (16)–(20) give rise to solutions of the Maxwell equations to leading paraxial approximation and coincide with the leading paraxial approximations given in [18] (upon neglecting spatial derivatives of their independent functions f and g).

2.4. OAM Waves as Particular Cases of Paraxial Approximation

Use will be made of electromagnetic waves with orbital angular momentum (OAM) with prescribed values of the integer parameters l, p (the integer l being allowed to be negative). They are generated by the functions $g_{l,p}$ given below.

Let $\rho = (x^2 + y^2)^{1/2}$ and for given $k_0 (> 0)$ in Equation (5), let:

$$g_{0,0} = (2/\pi)^{1/2} \exp[-\frac{\rho^2}{w(z)^2}] \exp[i\frac{z}{z_0}\frac{\rho^2}{w(z)^2}] f_{0,0}(\frac{z}{z_0}) \tag{21}$$

$$f_{0,0}(\frac{z}{z_0}) = \frac{w_0}{w(z)} \exp[-i \arctan \frac{z}{z_0}] \tag{22}$$

$$w(z) = w_0(1 + (z/z_0)^2)^{1/2}, z_0 = \frac{k_0 w_0^2}{2} \tag{23}$$

$$\epsilon_0 = \frac{w_0}{z_0} = \frac{2}{k_0 w_0} \tag{24}$$

ϵ_0 is different from (and, hence, should be not confused with) the dielectric permittivity of vacuum. $g_{0,0}$ corresponds to $l = 0$, $p = 0$. For general integer values of l, p, one considers the following functions (directly related to the Laguerre-Gauss (LG) functions $LG_{l,p}(\rho, z)$):

$$g_{l,p} = [\frac{p!}{(\mid l \mid + p)!}]^{1/2} L_p^{|l|}(\frac{2\rho^2}{w(z)^2})(\frac{2^{1/2}\rho}{w(z)})^{|l|} \times \exp i[l\phi - (2p + \mid l \mid) \arctan \frac{z}{z_0}] g_{00}$$

with $\phi = \arctan(y/x)$. $L_p^{|l|}(u)$ are the generalized Laguerre polynomials:

$$L_p^{|l|}(u) = \sum_{m=0}^{p} (-1)^m \frac{(\mid l \mid + p)!}{(p-m)!(\mid l \mid + m)! m!} u^m \tag{25}$$

A very important property of any $g_{l,p}$, for general integer l, p, is that:

$$\left(\nabla_{\bar{x}}^2 + 2ik_0 \frac{\partial}{\partial z}\right) g_{l,p} = 0 \tag{26}$$

The comparison of Equation (26) with Equation (14) shows that $g_{l,p}$ provides one important case of paraxial approximation. Then, in particular, one can always choose the components $A_{x,par}$ and $A_{y,par}$ of $\bar{A}_{par} (\simeq \bar{A}_{ex})$ to be equal to some suitable linear combination of $g_{l,p}$'s. Thus, the above $g_{l,p}$ yielding OAM electromagnetic waves provide one important example

of paraxial approximation. However, there are other cases of paraxial approximation which do not correspond to the above OAM electromagnetic waves.

3. Trapped Trajectories in Quasi-steady Laser Beams with OAM

In this section, results are reported about trajectories which are trapped in the plane transverse to the propagation direction of the laser beam. The physical effect behind this trapping is the ponderomotive force [24]. Such force is ubiquitous in any laser experiment with free charges but is only relevant for electrons inside strong laser fields. It expels electrons from the high intensity regions. For modes with a nodal axis, a tube of intensity is created. Moore calculated for the first time the possibility of electron confinement [25] inside such light tubes. Specifically, trapped trajectories are solutions to the relativistic Lorentz equation that perform a confined motion in the transverse xy plane, (not any sort of drifting motion in the latter). Compatibly with that, those trajectories may (do) acquire a net drift in the z direction and oscillate in a more or less complicated way in the transverse plane for many (typically for hundreds of) optical cycles.

We focus on the case of laser beams with net orbital angular momentum, namely $(l, p) = (1, 0)$ in our case, interacting with free electrons of initial kinetic energy equal to zero, except otherwise stated. Two case-studies will be analyzed in detail, one of a relatively wide laser beam spot, $w_0 = 100.0$ μm, the other of a narrow laser spot of $w_0 = 6.4$ μm. The beam waist, the f-number and λ_0 verify $w_0 = 0.87 \times \lambda_0 \times f\#$, hence the case of a small waist corresponds to f#/9.2 and it is a very common case in many of today's petawatt lasers with a long focal parabola. However, the case for the large waist corresponds to f#/143. This is an extremely long focus (probably to be achieved with a close to axis spherical mirror). In this case, keeping such intensity level over a so broad area will require probably a laser close to 40 PW at this mode, and using techniques as the indicated in [17] a power after compression close to 100 PW. This is one step beyond present day possibilities, but foreseen in the mid term at several world initiatives, as the Shanghai's Station of Extreme Light [1,26].

The rest of the parameters characterizing the laser are: $\lambda_0 = 800.0$ nm, $\chi_0 = -\pi$, $E_0 = 100 \times E_{atomic}/\sqrt{2}$ ($E_{atomic} = 5.14 \times 10^{11}$ V/m), electric field mainly polarized along the x-axis (that is, we choose $A_{x,par} \neq 0$, $A_{y,par} = 0$), the laser pulse is assumed to be much longer than the integration time to obtain the trapped solutions. Electrons are assumed to be located in all the cases at the beam waist position, i.e., at $z_0 = 0$, at $t_0 = 0$. From these values, the dimensionless laser parameter currently used in the literature, namely, $|q|A_0/(mc) = |q|E_0/(\omega_0 mc) = |q|E_0/(k_0 mc^2)$ can be defined, which turns out to be ≈ 9.0 in our case. This is indeed a large value, indicating the important role of nonlinearity in the simulations presented in the paper.

In both case-studies, a disk centered at the origin in the xy-plane of radius $w_0/20$ will be explored. Note that the region to be explored is well inside $w_0/\sqrt{2}$, the limit where the ponderomotive force tends to keep the electrons confined. Inside this zone, random initial conditions for the electrons will be generated, and subsequently integrated using the relativistic Lorentz equation with the exact paraxial fields discussed in earlier sections of the paper. Plots of the trajectory components, velocity components and eventually the relativistic γ factor will be provided to illustrate the main features of trapped solutions. The characterization of the set of trajectories as a whole will be obtained from their TS spectra, averaged at a selected detection point. As it is well known, the scattering of electromagnetic radiation by free charges is a standard diagnostic of their distribution functions (see for example [4,5] for applications in fusion plasmas), and also for the diagnosis of intense or ultra-intense laser beams.

It will be shown that in the case of wide laser spot, a Hamiltonian function can be introduced that substantially simplifies the equations of motion capturing at the same time many of the observed phenomena. As it will become clear in the discussion that follows, the main result is that B_z and E_z (the longitudinal field components) play an essential role

in accounting for the existence and character of these trapped solutions. Let us now begin a more detailed discussion of the two case-studies mentioned above.

3.1. Case-Study 1: Wide Laser Beam Spot, w_0 = 100.0 μm

Figure 1 shows four examples of trapped trajectories with initial conditions inside a circle or radius $w_0/20$ around the centre of the laser beam, see Table 1 for details. Two characteristics of these solutions seem clear: in the first place, the appearance of a relatively large, low frequency modulation of both the x and y coordinates of the electron, and on the second place the different amplitudes and phase relationship between these components for different initial conditions. Figures 2 and 3 show, respectively, the projection onto the xy plane and the velocity components for the trajectories in Figure 1: all of them show more or less pronounced modulations to the fast optical frequency, which should be traced back to the appearance of the above mentioned low frequency of dynamical origin.

Table 1. Sample initial conditions for trapped trajectories, case-study with $w_0 = 100$ μm.

x_0 [μm]	y_0 [μm]	z_0 [μm]
−1.5212	0.6148	0.0
−0.2693	0.2734	0.0
−0.3553	−2.2284	0.0
0.0596	−3.7369	0.0

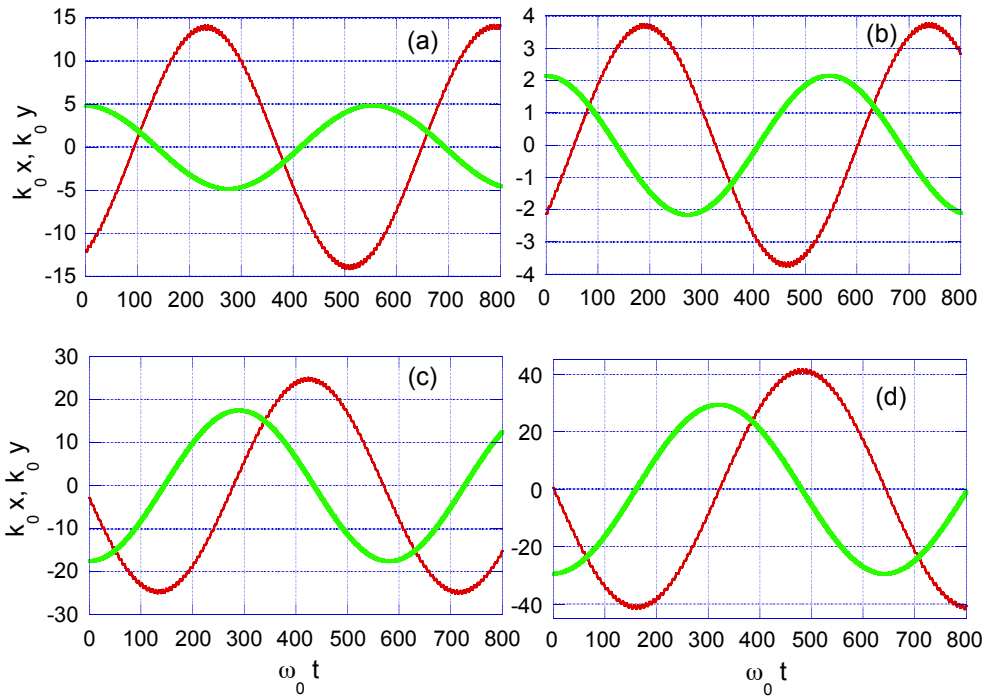

Figure 1. Temporal evolution of normalized $x(t)$ (in red) and $y(t)$ (in green). Abcissas and ordinates are dimensionless, being respectively the products $\omega_0 \times t$ and $k_0 \times x(t) = 2\pi x(t)/\lambda_0$, etc. Four cases with different initial conditions are displayed, see main text for details. Trapped solutions appear as low-frequency (as compared with the optical one) confined motions in the transverse xy-plane. Note the different relative phases and amplitudes of $x(t)$ and $y(t)$ depending on the initial conditions.

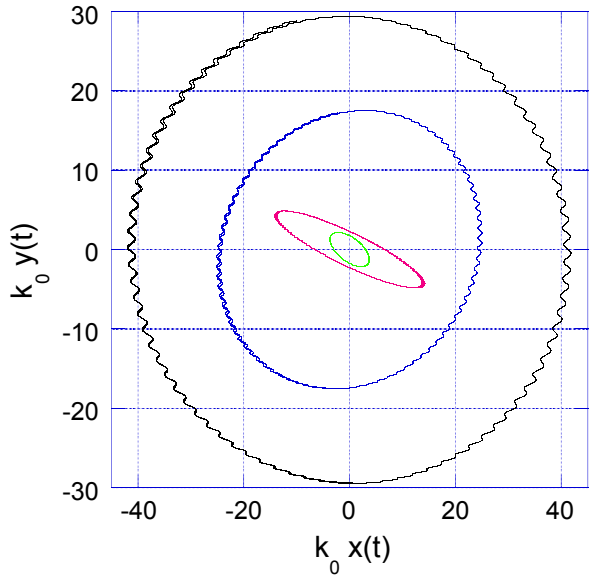

Figure 2. Parametric plots of normalized $y(t)$ vs. $x(t)$ for the cases of Figure 1. Color code is (a)-red, (b)-green, (c)-blue and (d)-black. $k_0 \times x(t)$ and $k_0 \times y(t)$ are dimensionless variables. The projection onto the xy-plane is (nearly) an ellipse, whose principal axes, overall amplitude and orientation depend on the initial conditions. All trajectories show besides a small oscillatory pattern due to the electron quiver motion.

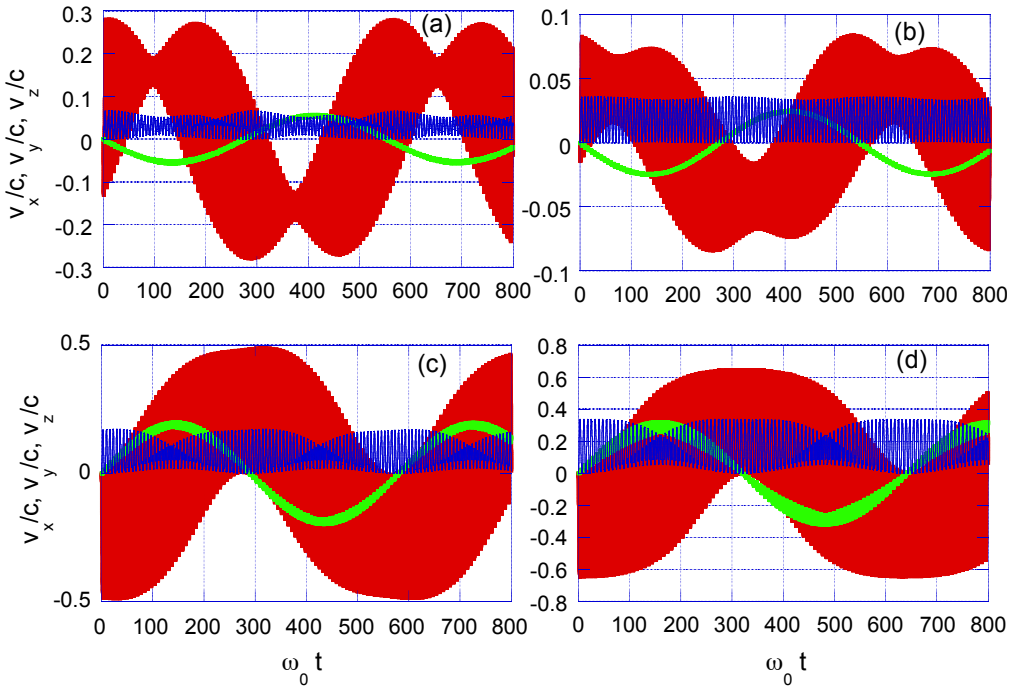

Figure 3. Time evolution evolution of $v_x(t)/c$ (in red), $v_y(t)/c$ (in green) and $v_z(t)/c$ (in blue). The same cases as in Figure 1 are displayed. The low-frequency modulation superimposed on transverse velocity components is apparent. v_z is also modulated, but with a net positive mean value, which accounts for the observed net drift of the trajectories in the positive z direction for $E_{kin0} = 0$.

It is easy to argue that to explain the observed modulations, it is essential to include the longitudinal field components $B_z(x, y, z, t)$ and $E_z(x, y, z, t)$. The argument is as follows: if we assume that the initial kinetic energy of the electron is zero, hence the initial values of

the velocity components are exactly zero at $t = 0$. But according to the relativistic Lorentz equation, written in terms of the acceleration

$$d\mathbf{v}/dt = (q/m)\sqrt{1 - \mathbf{v}^2/c^2}\Big(\mathbf{E} + \mathbf{v} \times \mathbf{B} - \mathbf{v}(\mathbf{v} \cdot \mathbf{E})/c^2\Big), \tag{27}$$

the time evolution of e.g. $v_y(t)$ is given by

$$dv_y/dt = (q/m)\sqrt{1 - \mathbf{v}^2/c^2}\Big(E_y + (v_z B_x - v_x B_z) - v_y(v_x E_x + v_y E_y + v_z E_z)/c^2\Big). \tag{28}$$

Now, if we set $E_y = 0, B_x = 0$ (electric field is assumed to be linearly polarized along the x-axis (no E_y component), and hence $\mathbf{B}$ is polarized along y-axis), and $B_z = 0$, $E_z = 0$ the previous equation would read

$$dv_y/dt = (q/m)\sqrt{1 - \mathbf{v}^2/c^2}\Big(-v_y(v_x E_x)/c^2\Big), \tag{29}$$

and it can be checked that $v_y(t) \equiv 0$ is indeed an exact solution of the previous equation, since its right-hand side evaluates to zero upon substituting $v_y(t) \equiv 0$, and the left-hand side (being the derivative of a constant) is also zero. Hence, any deviation of the y-component from its initial value, in particular any modulation appearing on it, must be accounted for by non-zero longitudinal components of the laser electromagnetic fields, in particular by a nonzero B_z in the case of y.

Trapped solutions which are born close to the laser beam axis ($\rho_0 = \sqrt{x_0^2 + y_0^2} \leq w_0/20$) are characterized by their TS averaged spectrum (over many independent realizations of electron trajectories). A detection point located 0.5 m along the y-axis, is chosen to compute the spectrum. With this geometry (approximate 90 degrees scattering) there are in general two possible contributions to the spectrum, namely along the x and z-axis. Taking into account that the laser electric field has been chosen to be polarized along the x-axis, it is expected that the spectrum is also highly polarized in that direction. Figure 4 shows the averaged spectrum over 2048 trajectories. It shows a main band approximately centered at $\omega/\omega_0 = 1$, but also substantial power at the second and third harmonics of this. The spectrum clearly shows the scattered radiation to be highly polarized along the x axis, the z component representing only 10% of the former one.

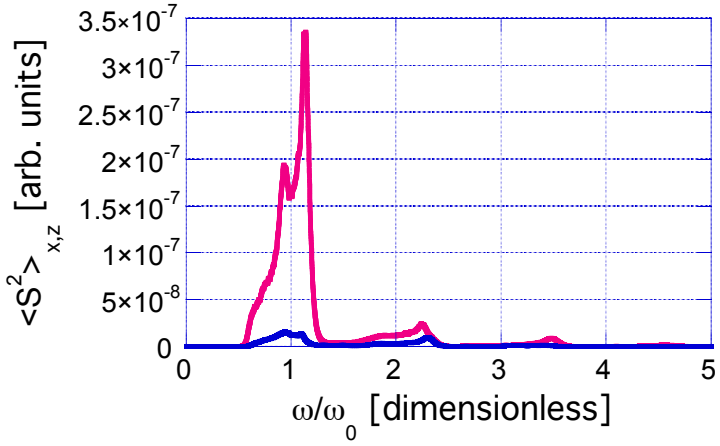

Figure 4. Averaged TS spectrum computed for a sample of 2048 trapped trajectories whose initial conditions are generated randomly inside a circle of radius $w_0/20$, $w_0 = 100.0$ μm. Averaged spectrum along x-axis is plotted in red, along z-axis in blue. The reference electric field of the ultra intense laser is $E_0 = 3.63 \times 10^{13}$ V/m. A rather broad spectral band around $\omega/\omega_0 = 1$ and less intense contributions at higher harmonics are apparent. Spectrum is strongly polarized along the x-axis in this case.

Let us now try an approach to the understanding of the trapped solutions based on simplified dynamical equations that capture the essential features of the problem. To do this, a first consideration is that the paraxial laser beam with net OAM we are considering has an equilibrium point at the laser beam centre, i.e., a point where electric and magnetic fields are zero. The idea is to obtain approximate equations of motion which are valid in a sufficiently small zone around the centre of the laser beam, and study them in order to obtain information for these trajectories.

Our starting point will be the general relativistic Hamiltonian of a free charged particle, acted on by completely general electric and magnetic fields, namely

$$H(x,y,z,t) = c\sqrt{(\mathbf{P}(x,y,z,t) - q\mathbf{A}(x,y,z,t))^2 + m_0^2c^2} + q\Phi(x,y,z,t) \tag{30}$$

where as usual $\mathbf{A}(x,y,z,t)$ and $\Phi(x,y,z,t)$ stand for the vector and scalar potentials, q is the charge of the particle, $\mathbf{P}$ is the canonical momentum and the $\mathbf{E}(x,y,z,t)$ and $\mathbf{B}(x,y,z,t)$ fields are obtained from the general rules in Equation (3). Now, take $A_y = 0$, $A_z = 0, A_x(x,y,z,t) = Re[A_{x,par}(x,y,z) \times \exp[i(k_0z - \omega_0t + \chi_0)]$ with $A_{x,par}(x,y,z) = g_{1,0}(x,y,z)$ and $\Phi(x,y,z,t) = Re[\Phi_{par}(x,y,z) \times \exp[i(k_0z - \omega_0t + \chi_0)]$, $\Phi_{par}(x,y,z) = -\frac{ic^2}{\omega_0}\frac{\partial}{\partial x}g_{1,0}(x,y,z)$, according to the rules stated above. Then, a series expansion is made (with the help of the computer algebra system Mathematica^{TM}) keeping terms to quadratic order in any of the dimensionless variables $\pi_x = P_x/mc, \pi_y = P_y/mc, \pi_z = P_z/mc$, $X = k_0x, Y = k_0y, Z = k_0z$. The sine and cosine functions, including the propagating phase term $\psi = \psi(z,t) = k_0z - \omega_0t + \chi_0 = Z - \tau + \chi_0$, are kept unexpanded: they will act as a kind of (non-autonomous) forcing terms in the canonical equations thus obtained.

The normalized Hamiltonian $h(\pi_x, \pi_y, \pi_z, X, Y, Z, \tau) = H(P_x, P_y, P_z, x, y, z, t)/mc^2$, $\tau = \omega_0t$, keeping terms up to (maximum) second order in any product of the canonical variables, is given explicitly as:

$$\left(\frac{1}{2}\left(\pi_x^2 + \pi_y^2 + \pi_z^2 + \frac{\alpha^2[X\cos(Z-\tau+\chi_0) - Y\sin(Z-\tau+\chi_0)]^2}{k_0^2w_0^2} - \right.\right.$$
$$\frac{2\alpha[X\cos(Z-\tau+\chi_0) - Y\sin(Z-\tau+\chi_0)]\pi_x}{k_0w_0} -$$
$$\left.\left.\frac{2\alpha\left[2XY\cos(Z-\tau+\chi_0) + \left(3X^2 + Y^2 - k_0^2w_0^2\right)\sin(Z-\tau+\chi_0)\right]}{k_0^3w_0^3}\right)\right) \tag{31}$$

The corresponding canonical equations for Equation (31) are written below, and turn out to depend solely on a dimensionless parameter having to do with the laser intensity, labelled α and on the dimensionless product k_0w_0. For a fixed wavelength and a fixed laser intensity, the behavior of the trapped solutions is determined hence by the size of the laser beam spot size, which is the parameter explored in this investigation.

$$dX/d\tau = \pi_x - \frac{\alpha}{k_0 w_0}(X\cos\psi - Y\sin\psi), \tag{32}$$

$$dY/d\tau = \pi_y, \tag{33}$$

$$dZ/d\tau = \pi_z, \tag{34}$$

$$d\pi_x/d\tau = \frac{\alpha\pi_x\cos\psi}{k_0 w_0} - \frac{\alpha^2\,(X\cos\psi - Y\sin\psi)\cos\psi}{k_0^2 w_0^2} + \frac{2\alpha(Y\cos\psi + 3X\sin\psi)}{k_0^3 w_0^3}, \tag{35}$$

$$d\pi_y/d\tau = -\frac{\alpha\pi_x\sin\psi}{k_0 w_0} + \frac{\alpha^2(X\cos\psi - Y\sin\psi)\sin\psi}{k_0^2 w_0^2} + \frac{2\alpha(X\cos\psi + Y\sin\psi)}{k_0^3 w_0^3}, \tag{36}$$

$$d\pi_z/d\tau = -\frac{\alpha\pi_x(X\sin\psi + Y\cos\psi)}{k_0 w_0} + \frac{\alpha^2(X\sin\psi + Y\cos\psi)(X\cos\psi - Y\sin\psi)}{k_0^2 w_0^2} - \frac{\alpha(2XY\sin\psi + (k_0^2 w_0^2 - (3X^2 + Y^2))\cos\psi)}{k_0^3 w_0^3}. \tag{37}$$

To test whether these equations can capture the main features of trapped trajectories for the case study at hand, Figure 5 gives a representative example of two sample trajectories that are born quite close to the laser beam origin, computed from the numerical solution of the full relativistic Lorentz equation and from the canonical equations above. Quantitative agreement is very good, allowing to predict the low frequency modulation of the transverse variables, and how their amplitudes and mutual phase depend on the initial conditions.

The approximate Equation (31) has the structure of a non-relativistic Hamiltonian. Then, one would expect that it may be an unreliable approximation when the electron separation from the origin of coordinates increases and/or the electron velocities increase towards c.

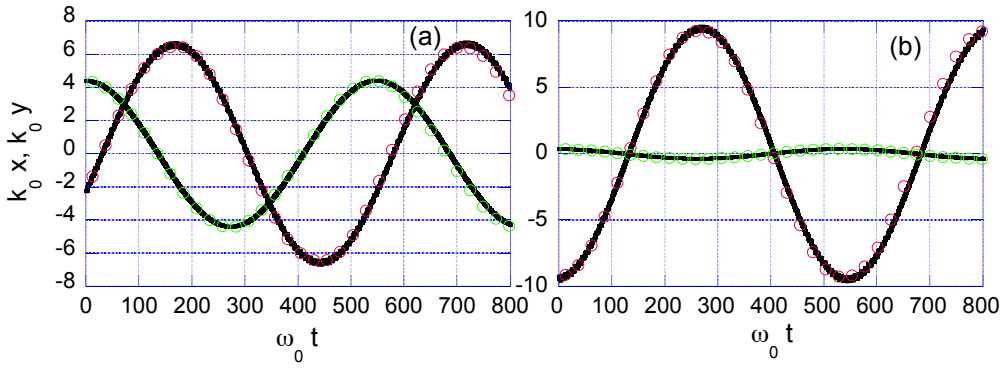

Figure 5. Temporal evolution of normalized $x(t)$ and $y(t)$ from full paraxial laser fields (thick black lines) and from the approximate Hamiltonian, unfilled red ($x(t)$) and green ($y(t)$) circles. Two cases are displayed: (**a**) the initial conditions are $x_0 = -0.287747$, $y_0 = 0.5596$ [μm], (**b**) the initial conditions are $x_0 = -0.287747$, $y_0 = 0.5596$ [μm]. In both cases $z_0 = 0$ and $E_{kin0} = 0$. Good quantitative agreement is found as regards the modulation frequency, amplitude and mutual phase of transverse coordinates.

3.2. Case-Study 2: Narrow Laser Beam Spot, w_0 = 6.4 μm

Figures 6 and 7 show four examples of trapped trajectories with initial conditions inside a circle or radius $w_0/20$ around the centre of the laser beam (see Table 2 for details).

Table 2. Sample initial conditions for trapped trajectories, case-study with $w_0 = 6.4$ μm.

x_0 [μm]	y_0 [μm]	z_0 [μm]
−0.2185	0.2189	0.0
0.1244	−0.069	0.0
0.2846	−0.1308	0.0
0.1123	−0.072	0.0

The first characteristic to note about trapped solutions in this case study, differing markedly from case study 1, is their rather complex temporal behavior, perhaps more easily seen in terms of the velocity components and the $\gamma(t)$ factor (Figures 8 and 9). The oscillations in the transverse plane proceed at a much faster characteristic frequency than in case-study 1 treated before. It seems clear that the growing amplitudes of the B_z and E_z components, that scale with the dimensionless parameter $1/(k_0 \times w_0)$, play a key role in this connection.

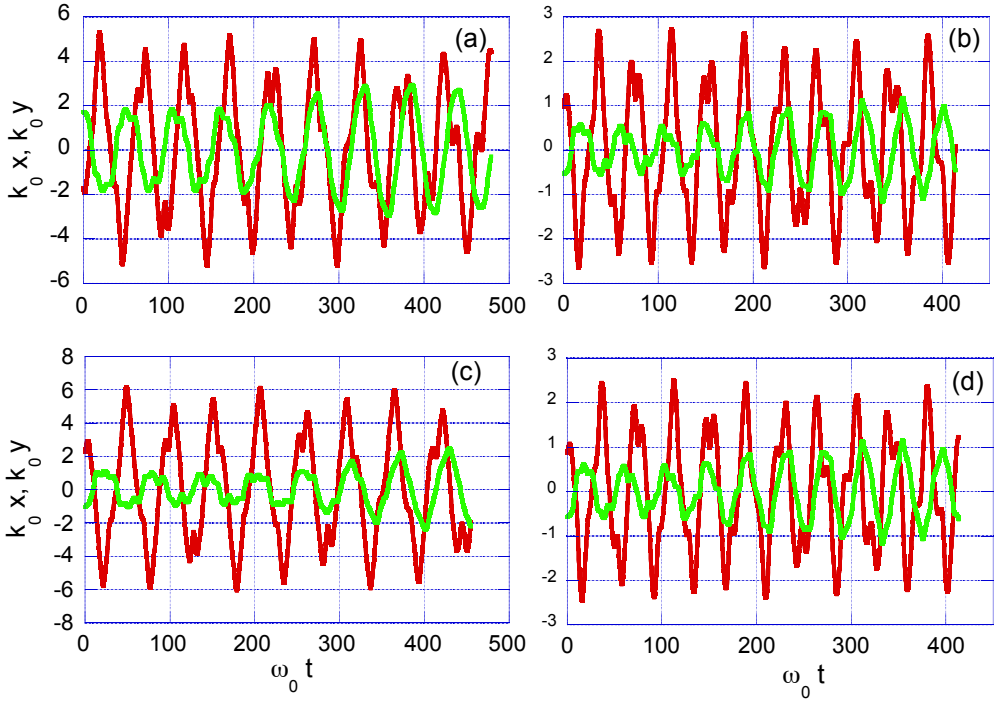

Figure 6. Temporal evolution of normalized $x(t)$ (in red) and $y(t)$ (in green). Abcissas and ordinates are dimensionless, being respectively the products $\omega_0 \times t$ and $k_0 \times x(t) = 2\pi x(t)/\lambda_0$, etc. Four cases with different initial conditions are displayed, see main text for further details. Trapped solutions are apparent as confined motions in the transverse $x - y$ plane. The characteristic frequencies of these trapped solutions are much higher than in case-study 1 and they have a more complex temporal behaviour.

A parametric plot of the trajectories' projection onto the xy plane shows them to become quite complex with decreasing w_0. Of course, the character of the movements (whether they are quasi periodic or even chaotic for some combination of the parameters) cannot be ascertained simply from those plots. A more extensive numerical study of these aspects lies outside the scope of this paper, and should be addressed elsewhere.

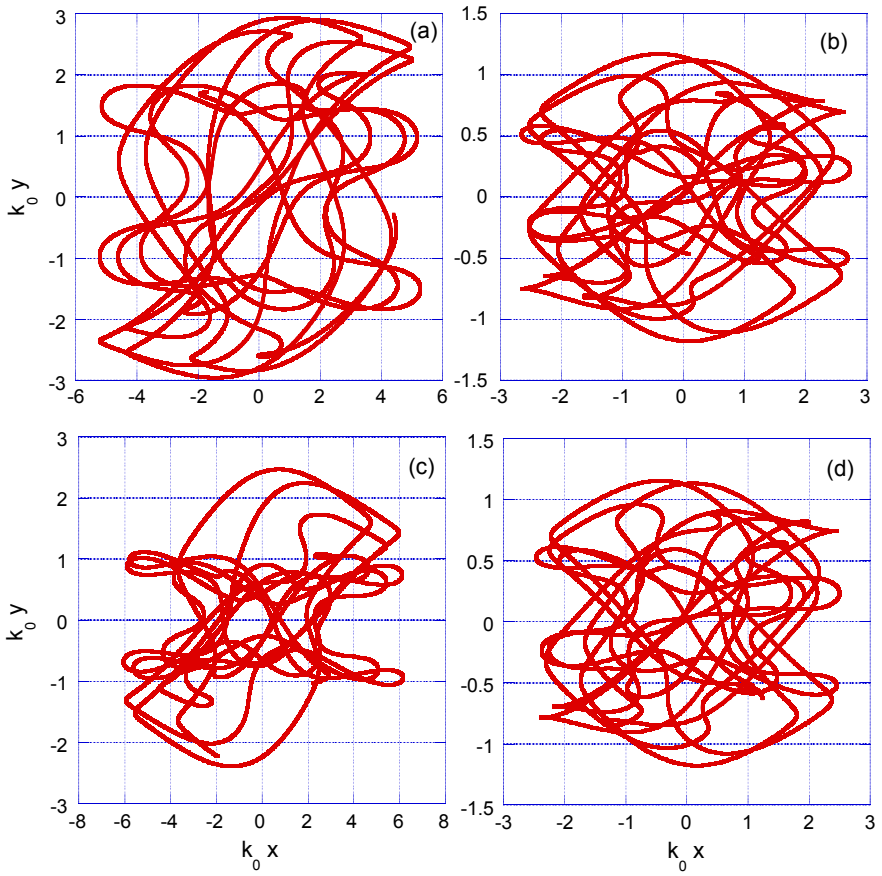

Figure 7. Parametric plots of normalized $y(t)$ vs. $x(t)$ in the four cases of Figure 6. $k_0 \times x(t)$ and $k_0 \times y(t)$ are dimensionless variables. Projections of trajectories onto the xy-plane are considerably more complex than in case-study 1, compare with Figure 2.

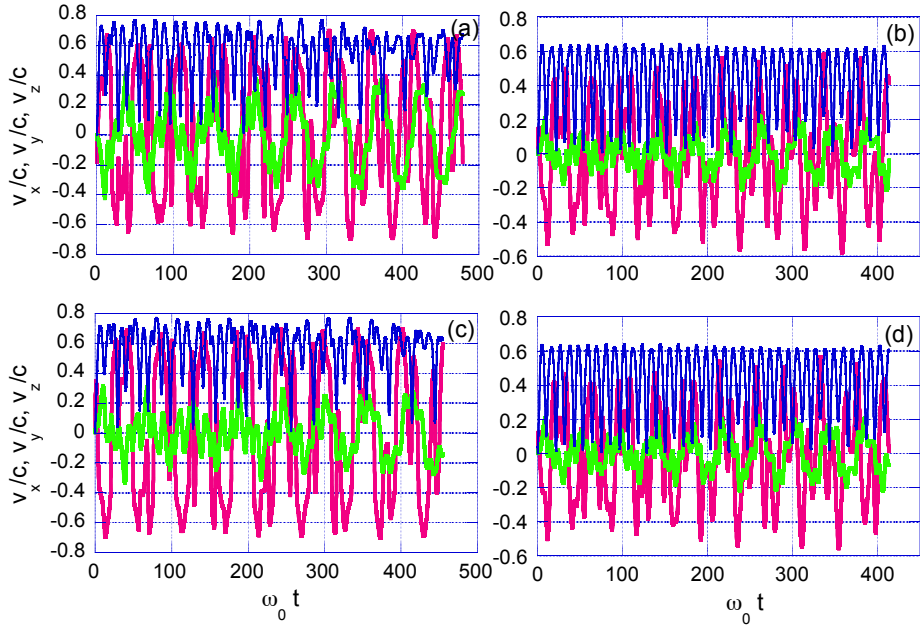

Figure 8. Temporal evolution of $v_x(t)/c$ (in red) and $v_y(t)/c$ (in green) and $v_z(t)/c$ (in blue). The same cases as in Figure 6 are displayed.

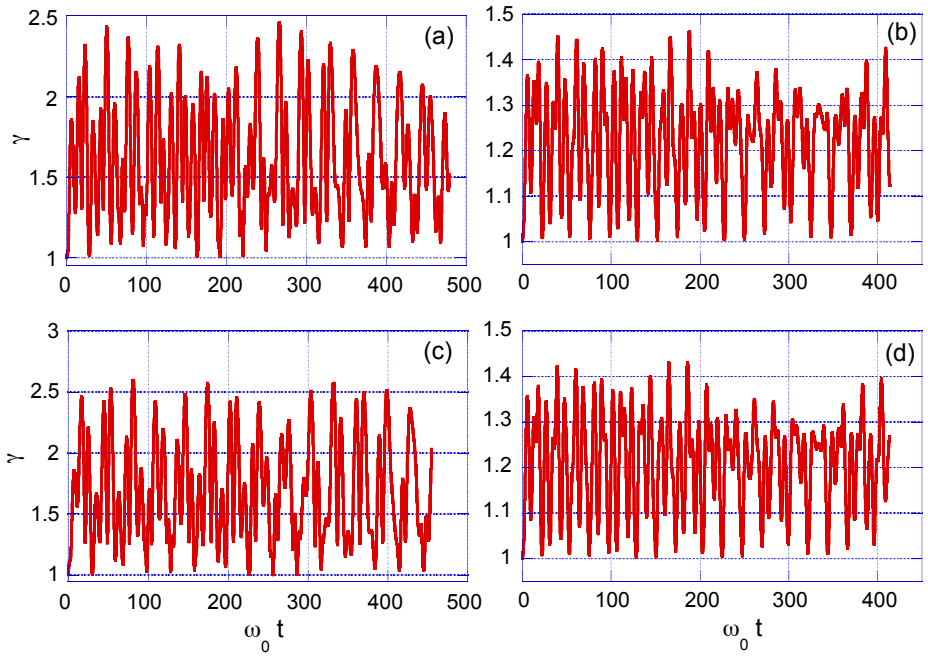

Figure 9. Time evolution of $\gamma(t)$ for the cases displayed in Figure 6. As in previous plots, temporal axis is displayed in terms of the dimensionless variable $\omega_0 \times t$.

As in case-study 1 in the previous subsection, trapped solutions are also characterized here by their TS spectrum, averaged over many independent realizations of electron trajectories. A detection point located 0.5 m from the beam centre, along the y axis, is chosen to compute the spectrum. Figure 10 shows the averaged spectrum, featuring an overall shift towards lower frequencies in this case (as compared with case-study 1), the appearance of spectral peaks at rather low frequencies, and a more balanced contribution of its x and z quadratures.

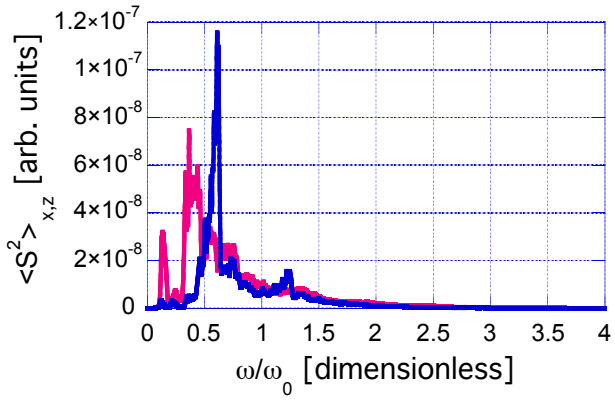

Figure 10. Averaged TS spectrum computed for a sample of 1024 trapped trajectories whose initial conditions are generated randomly in a circle of radius $w_0/20$ around the laser beam axis. Averaged spectrum along x-axis is plotted in red, along z-axis in blue. Spectrum shows an overall shift towards lower frequencies in this case as compared with case study 1, and a more balanced contribution of its x and z quadratures.

4. Electron Dynamics in Ultrashort-Pulse, Paraxial Laser Beams with OAM

In this section, we report results about electron dynamics in genuine ultrashort laser pulses with paraxial OAM fields. The fields are in this case

$$\bar{E}_{par} = i\omega_0 \bar{A}_{par,0} \times e^{-(\frac{k_0 z - \omega_0 t - k_0 z_{0p}}{\omega_0 T_p})^2} \quad (38)$$

$$E_{z,par} = -ik_0 \Phi_{par,0} \times e^{-(\frac{k_0 z - \omega_0 t - k_0 z_{0p}}{\omega_0 T_p})^2} \quad (39)$$

$$B_{x,par} = -ik_0 A_{y,par,0} \times e^{-(\frac{k_0 z - \omega_0 t - k_0 z_{0p}}{\omega_0 T_p})^2} \quad (40)$$

$$B_{y,par} = ik_0 A_{x,par,0} \times e^{-(\frac{k_0 z - \omega_0 t - k_0 z_{0p}}{\omega_0 T_p})^2} \quad (41)$$

$$B_{z,par} = (\frac{\partial}{\partial x} A_{y,par,0} - \frac{\partial}{\partial y} A_{x,par,0}) \times e^{-(\frac{k_0 z - \omega_0 t - k_0 z_{0p}}{\omega_0 T_p})^2} \quad (42)$$

where T_p defines the temporal width of the laser pulse and z_{0p} the center of the gaussian envelope at the initial time $t = 0$. $T_p = 8 \times \lambda_0/c$ and $z_{0p} = -24 \times \lambda_0$ are chosen in the computations. T_p is connected with the temporal FWHM of the pulse by the simple relation FWHM = $2\sqrt{(\ln 2)}Tp$, and is equal to 35.52 [fs] in our case. We now impose $A_{y,par}, 0 = 0$. $A_{x,par,0}, \Phi_{par,0}$ are respectively equal to $A_{x,par}, \Phi_{par}$ in Section 3, except for the factor $e^{-(\frac{k_0 z - \omega_0 t - k_0 z_{0p}}{\omega_0 T_p})^2}$, which has been displayed explicitly for convenience. The laser parameters are also the same as in Section 3. The electrons are located initially at $z_0 = 0$, hence very far away from the center of the Gaussian envelope, and in all cases $E_{kin0} = 0$. Their transverse distribution is discussed below. The physical picture is that of an ultra-intense laser pulse that propagates towards the electron and the transient dynamics is studied. We look for specific effects related with the OAM pulsed fields, either with their transverse structure or the presence of longitudinal fields.

A convenient tool to investigate those effects that are genuinely associated to the paraxial characteristics of the laser fields, is the analytical solution found for the electron dynamics in a Gaussian pulsed plane wave (Appendix A). That analytical solution is completely general as regards the intensity of the electromagnetic field or the energy and initial position of the electron, but it considers neither any structure transverse to the propagation direction nor any longitudinal fields. But it turns out, nevertheless, that in some specific cases, the analytical solution in Appendix A provides an excellent quantitative fit to the more complex paraxial dynamics. Hence, we have the opportunity to contrast the analytical solution against the paraxial one, in order to clarify the role of the different mechanisms leading to the observed dynamics.

We study two cases, one of a wide laser beam spot, $w_0 = 100.0$ μm and the other of a narrow laser beam spot $w_0 = 6.4$ μm.

4.1. Case-Study 1: Pulsed Laser with Wide Beam Spot, w_0 = 100.0 μm

We find that electrons initially located at $\rho_0 = \sqrt{x_0^2 + y_0^2} = w_0/\sqrt{2}$ (or very close to it) in the transverse plane and $z_0 = 0$ are amenable to an excellent fit with the analytical solution, see Figure 11 for the case $x_0 = w_0/\sqrt{2}, y_0 = 0$. For other values of $x_0 \in [-1.5 \times w_0, 1.5 \times w_0]$ ($y_0 = 0$), the observed discrepancies of the paraxial solution with the analytical one arise because the electron acquires (asymptotically) in general non-vanishing values for v_x and v_z, hence a substantial kinetic energy from the laser field, see Figure 11. If initial conditions of the form $x_0 = 0, y_0 \in [-1.5 \times w_0, 1.5 \times w_0]$ are considered instead, the electron acquires in general asymptotic non-vanishing values for v_y and v_z. In particular, an asymptotic $v_y \neq 0$ is directly related with the longitudinal paraxial fields being different from zero. Hence, it is impossible that this behavior be modeled by the analytical solution: see Figure 11.

That the paraxial behavior cannot, in general, be modeled by the pulsed analytical solution is easy to see. Consider for example, the asymptotic value of the kinetic energy according to the latter one, which is found to be:

$$m_0c^2\left(\sqrt{1+\frac{f_{10}^2+f_{20}^2+\frac{(m_0^2c^2-\gamma_1^2)^2+f_{10}^2+f_{20}^2}{4\gamma_1^2}}{m_0^2c^2}}-1\right) \tag{43}$$

where

$$f_{10} = p_{x0} + qA_x(t=0, z=0) \tag{44}$$

$$f_{20} = p_{y0} + qA_y(t=0, z=0) \tag{45}$$

$$\gamma_1 = \sqrt{m_0^2c^2 + p_{x0}^2 + p_{y0}^2 + p_{z0}^2} - p_{z0} \tag{46}$$

As we are assuming that the initial kinetic energy of the electrons is zero, and that the electric field is polarized along the x-axis one gets $p_{x0} = p_{y0} = p_{z0} = 0$, $f_{10} = qA_x(t=0, z=0)$, $f_{20} = 0$, $\gamma_1 = m_0c$. Considering the very low contribution of the term $qA_x(t=0, z=0)$ in our case (the electron is located very far away from the center of the gaussian pulse), the asymptotic kinetic energy would be essentially zero in all cases, no matter how large the maximum value of $\gamma(t)$ is in the course of the interaction with the gaussian plane wave pulse (Lawson-Woodward theorem). This proves that a good fit between the paraxial and analytical solutions is not to be expected, since the former predicts a substantial increase of the kinetic energy of the electron (in general) after the pulse has overtaken it, and the latter not.

But note that this could be radically changed if the electron initial position with respect to the plane pulsed wave is changed, so that the contributions from qA_x (and eventually qA_y) is significant. In that case, the analytic pulsed solution shows that the asymptotic value of E_{kin} depends not only on the initial momentum of the electron, but also on the amplitude and phase of the vector potential at its initial position. For ultra-intense lasers this contribution can be very high in absolute terms, although small if compared with the peak values of the pulsed field, and one can have a net energy change of the electron.

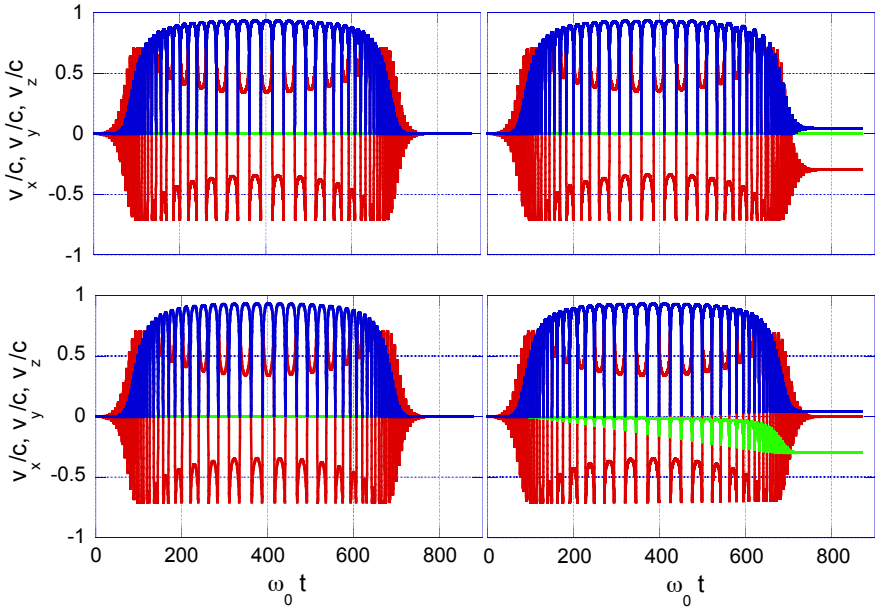

Figure 11. Left column, temporal evolution of velocity components for paraxial fields (top panel) versus analytical solution (bottom panel), $x_0 = w_0/\sqrt{2}, y_0 = 0$: quantitative agreement is excellent in this case. Right column, top panel, $x_0 = 65.0$ μm, $y_0 = 0$. bottom panel, $y_0 = 65.0$ μm, $x_0 = 0$. No precise quantitative match with the analytical solution is found now. Color code is red, green and blue for v_x/c, v_y/c and v_z/c respectively. Temporal axis is given as the dimensionless product $\omega_0 \times t$.

The asymptotic values for the final kinetic energy of the electrons have been studied as a function of their initial positions across the laser beam. For that purpose, we generate random initial conditions uniformly distributed across the laser beam up to a maximum radius of $1.5 \times w_0$. The resulting distribution turns out to have a non-trivial rotational symmetry around the optical axis, that is broken to a lower one if the contributions of axial fields E_z and B_z are set to zero in the numerical simulations. The maximum value of asymptotic kinetic energy is found to be 472.11 keV for a sample of 2048 initial conditions, see Figures 12 and 13.

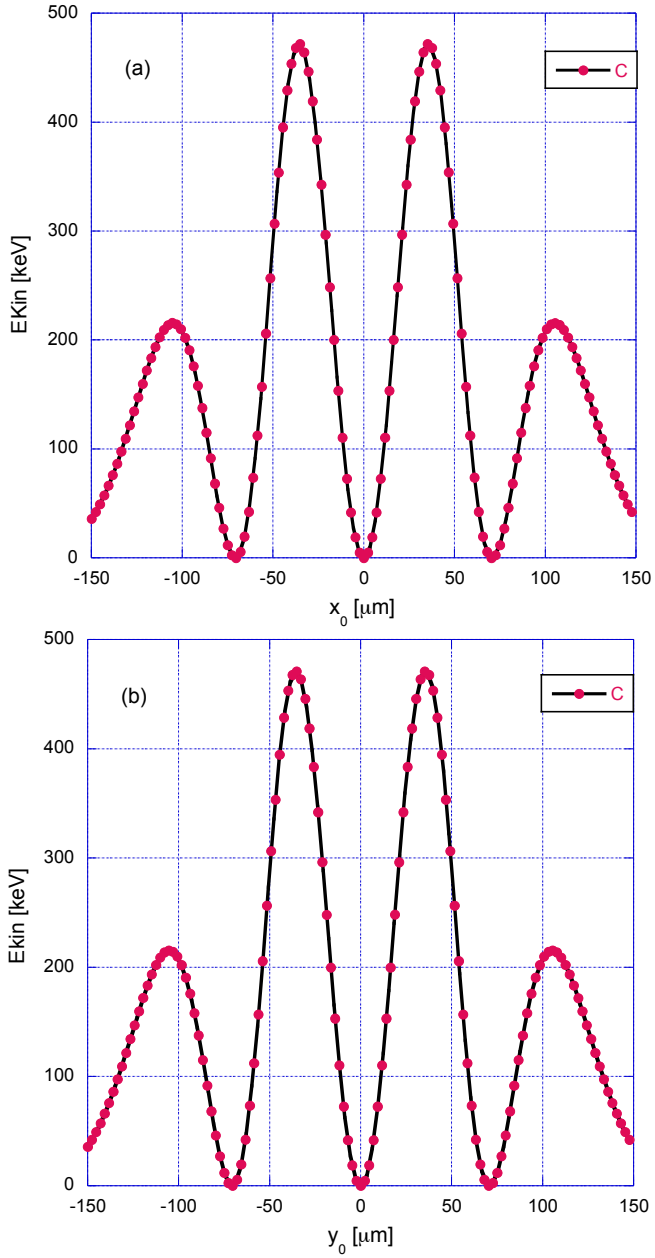

Figure 12. Asymptotic values of the kinetic energy for initial conditions of the form $x_0 \in [-1.5 \times w_0, 1.5 \times w_0]$, y_0 random $\in [-\lambda_0/2, \lambda_0/2]$, $z_0 = 0$ (a), and $y_0 \in [-1.5 \times w_0, 1.5 \times w_0]$, x_0 random $\in [-\lambda_0/2, \lambda_0/2]$, $z_0 = 0$ (b). Red dots correspond to the computations, black lines are cubic spline fittings to the data. The 90° symmetry of the asymptotic kinetic energy distribution is apparent from this figure.

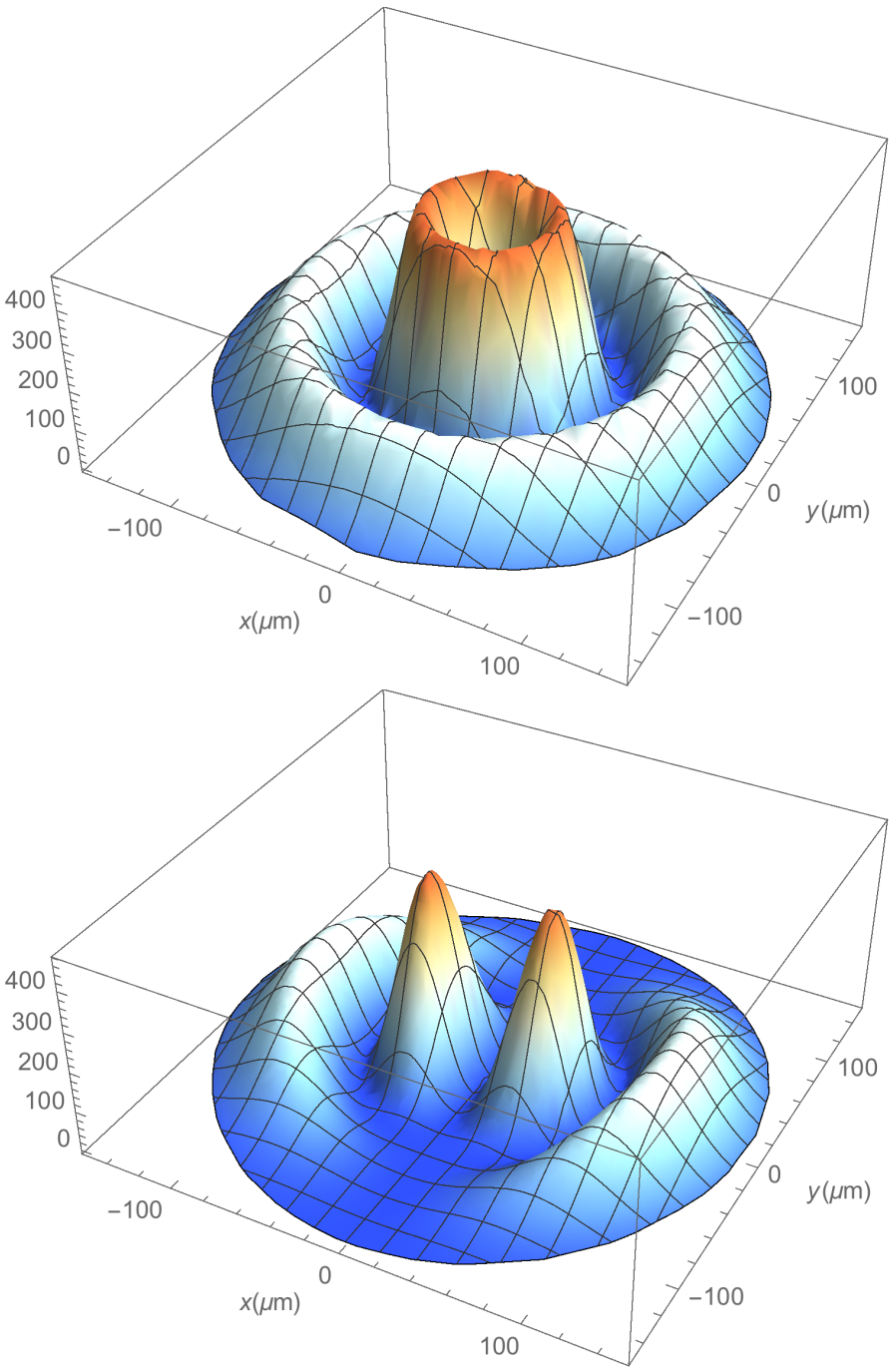

Figure 13. Top panel, 3D asymptotic kinetic energy plot for an uniform random distribution of initial conditions fulfilling $\rho_0 = \sqrt{x_0^2 + y_0^2} \leq 1.5 \times w_0$ and full paraxial fields. Vertical axis units are keV. Its rotational symmetry around the propagation axis is apparent. Bottom panel, the same as top one, except for longitudinal fields set to zero. Now the symmetry is lowered, although distributions coincide along the polarization axis.

4.2. Case-Study 2: Pulsed Laser with Narrow Beam Spot, w_0 = 6.4 µm

This case differs substantially from the previous one in several respects: on the one side, the (pulsed) temporal evolution is less ordered, and no clear quantitative match of the paraxial solution and the analytical solution is found, see Figures 14 and 15. A fraction of the initial conditions studied (randomly distributed inside a circle of radius $1.5 \times w_0$) leads the electron to leave the laser spot quite fast, consequently acquiring a very large final kinetic energy.

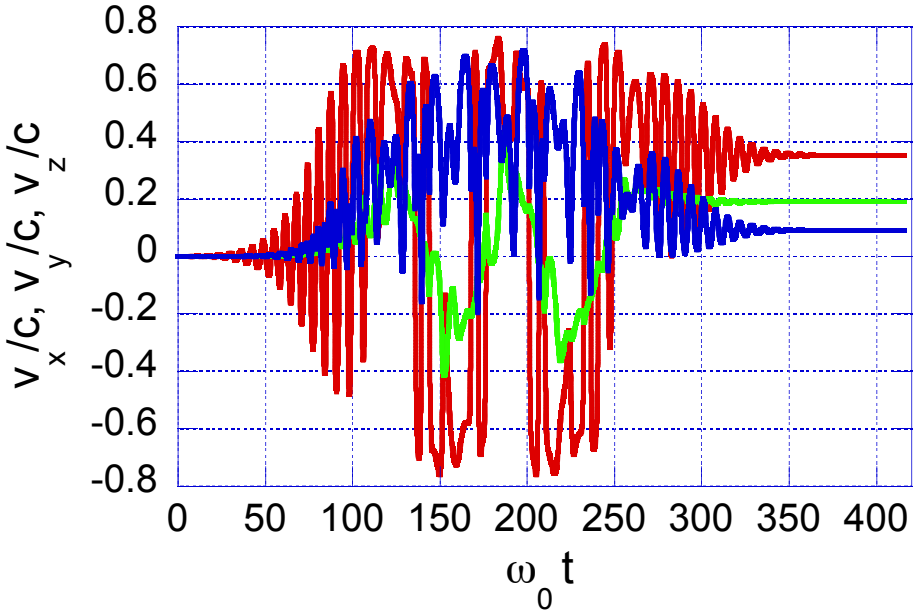

Figure 14. Time evolution of velocity components for $x_0 = -1.60859$ µm, $y_0 = -0.6644$ µm, $z_0 = 0$. A complex pulsed dynamics is found in this case. After the interaction with the laser pulse the electron acquires non-vanishing asymptotic velocity components on all coordinates axes in general. Color code is red, green and blue for v_x/c, v_y/c and v_z/c respectively. Temporal axis is given as the dimensionless product $\omega_0 \times t$.

The asymptotic kinetic energy of the electron has also been studied in this case as a function of the initial position across the laser beam. Initial conditions uniformly distributed across the laser beam up to a maximum radius of $1.5 \times w_0$ have been generated. The resulting distribution turns out also to have a non-trivial rotational symmetry around the optical axis (substantially different in shape from the one in the former case) and with a maximum value (in a sample of 16384 initial conditions) equal to 3.74 MeV, see Figures 16 and 17.

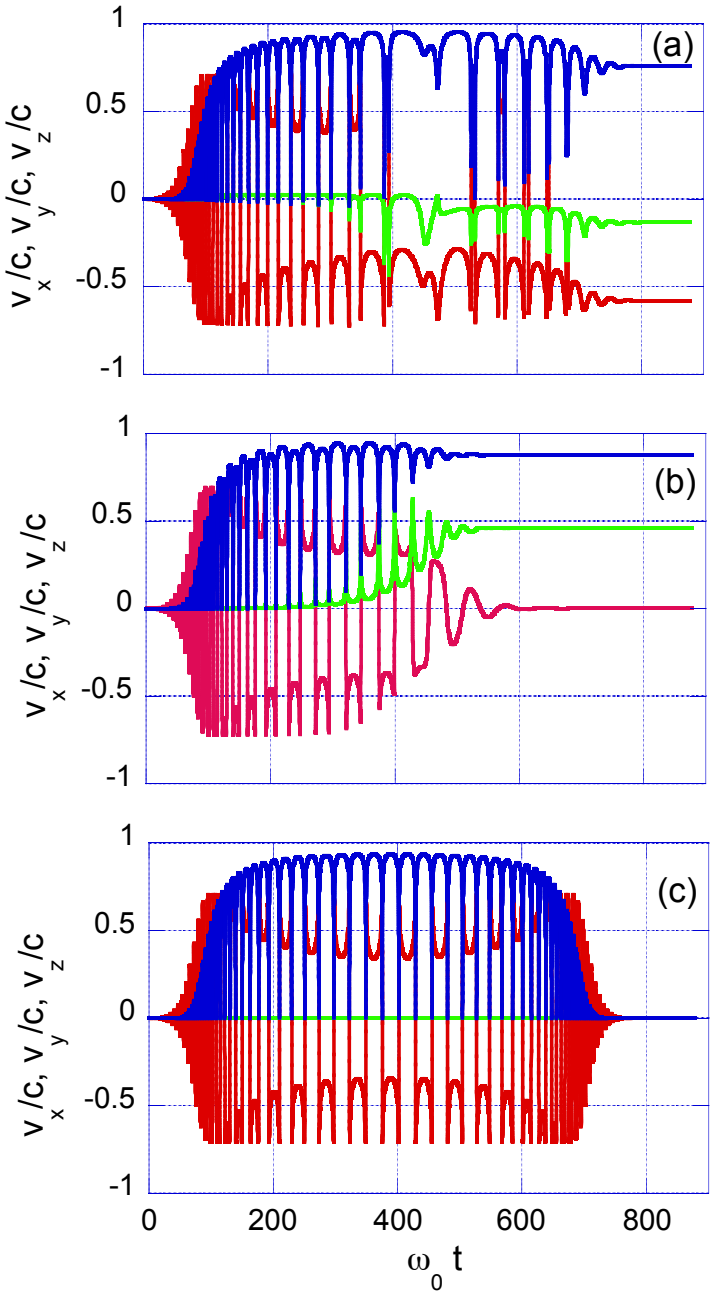

Figure 15. Time evolution of velocity components for paraxial fields (top and medium panels) versus analytical solution (bottom panel). Initial conditions on top panel are $x_0 = w_0/\sqrt{2}$, $y_0 = 0, z_0 = 0$ and in medium panel $y_0 = w_0/\sqrt{2}, x_0 = 0, z_0 = 0$. No quantitative agreement with the analytical solution is found in this case. Color code is red, green and blue for v_x/c, v_y/c and v_z/c respectively. Temporal axis is given as the dimensionless product $\omega_0 \times t$.

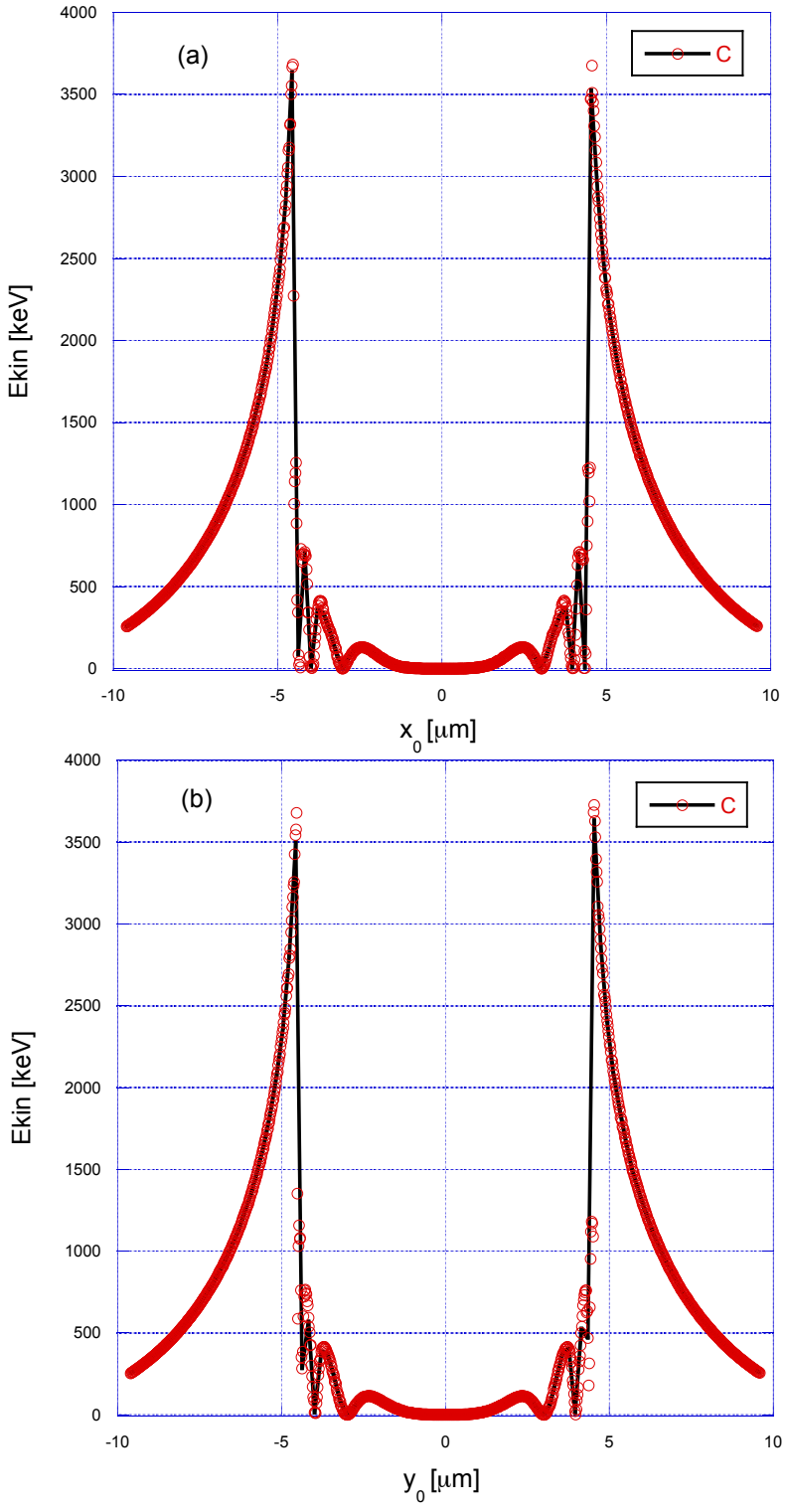

Figure 16. Asymptotic values of the kinetic energy for initial conditions of the form $x_0 \in [-1.5 \times w_0, 1.5 \times w_0]$, $y_0 \in [-\lambda_0/2, \lambda_0/2]$, $z_0 = 0$ (**a**), and $y_0 \in [-1.5 \times w_0, 1.5 \times w_0]$, $x_0 \in [-\lambda_0/2, \lambda_0/2]$, $z_0 = 0$ (**b**). $w_0 = 6.4$ μm in this case. Red circles correspond to the computed initial conditions, black lines are cubic spline fittings to the data. Note that the two prominent peaks of E_{kin} are very close to $\pm w_0/\sqrt{2}$, the region where the OAM mode with $(l, p) = (1, 0)$ is known to trap electrons due to the ponderomotive force. The 90° symmetry of the asymptotic kinetic energy distribution is apparent from this figure.

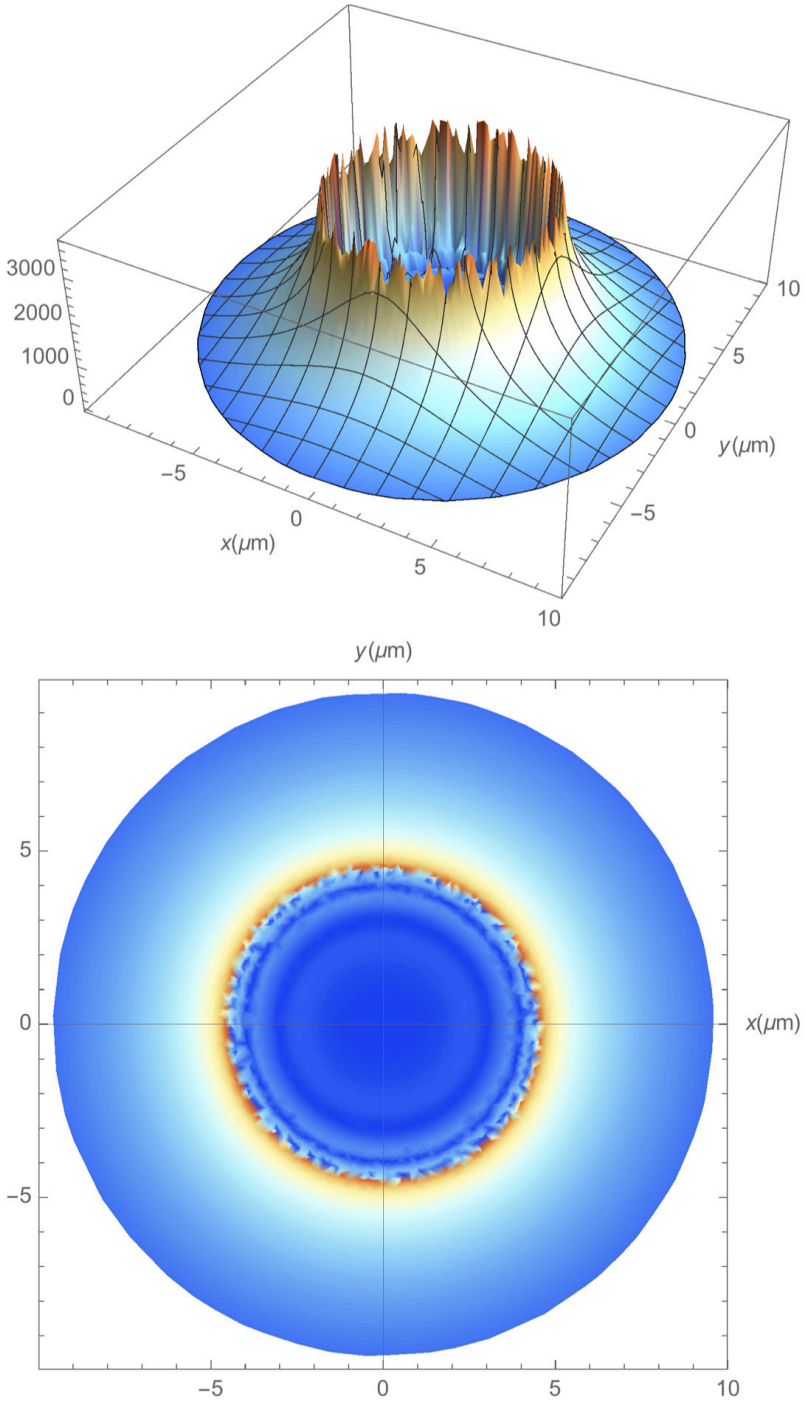

Figure 17. (**Top**) panel, 3D plot of the asymptotic kinetic energy for an uniform random distribution of initial conditions fulfilling $\rho_0 = \sqrt{x_0^2 + y_0^2} \leq 1.5 \times w_0$ and full paraxial fields. Vertical axis units are keV. (**Bottom**) panel, the 2D density plot of top panel. The distribution shows rotational symmetry around the propagation axis, but very different shape and maximum kinetic energy as compared with the $w_0 = 100.0$ μm case.

5. Conclusions and Discussions

Our approach in this paper employs the Lorentz gauge (namely, non-vanishing vector and scalar potentials) for describing the electromagnetic field and, moreover, the Lorentz condition. One generic advantage of such a framework is a systematic treatment of the paraxial approximation and the corrections to it. Upon identifying clearly the vector poten-

tial and the scalar potential of the paraxial field, our method has, in particular, the following advantage: it allows, at a later stage, a systematic approximation of the full relativistic Hamiltonian for the electron by a simpler form, capturing the main phenomenology of trapped solutions, for instance.

The numerical experiments in this paper show, in particular, that the "extra" terms appearing in [18] (the lowest corrections to the paraxial approximation in their method), as compared to our approach, have a negligible influence in the studies reported here. Hence, those extra terms are of extremely small magnitude.

In Section 3, the paper presents results on electron dynamics in ultra-intense paraxial laser beams with net orbital angular momentum (OAM). The paper elucidates the nature and conditions for so called trapped solutions, that is, solutions that are bounded in the transverse plane of the laser and drifting, in general, along the propagation direction. The influence of laser parameters on them, in particular the laser beam size and the non-vanishing longitudinal field components, essential for the paraxial approximation to be fulfilled, is studied. When the initial conditions of the electrons are sufficiently close to the origin, a simplified model Hamiltonian to the full relativistic one is introduced, depending basically on the dimensionless combination $k_0 w_0$ for fixed laser intensity. The results from this simplified Hamiltonian compare quite well quantitatively with the observed amplitudes, phase relationships and frequencies of oscillation of trapped solutions, at least for the case of wide laser beam size, $w_0 = 100.0$ μm.

Section 4 is devoted to ultrashort-pulse paraxial laser beams with OAM, including also a comparison of the paraxial dynamics with the results of the analytical solution for a pulsed plane wave with Gaussian envelope, given in Appendix A.

In Appendix A, we obtain an exact analytical solution of the electron dynamics in a pulsed plane wave with a Gaussian envelope. The solution is valid for any field intensity or initial energy of the electron and its predictions are compared with the dynamics in more complex paraxial fields with OAM. In some cases that are quantitatively characterized, the analytical model is an excellent approximation to the paraxial dynamics. Departures from the analytical solution are traced back to the combined influence of the transverse structure of the laser field and the longitudinal E_z and B_z components whose influence scale with the inverse of the laser beam size. It is argued that one of the limitations of the analytical solution to fit the paraxial one (in the particular set up studied in this paper) is the very small contribution of the laser fields at the initial position of the electron. A comparison of the paraxial and analytical solutions in a set-up where the effect of $qA_x(t = 0, z = 0), qA_y(t = 0, z = 0)$ is not negligible can contribute to gain some analytical insight into paraxial dynamics, but this issue should be addressed elsewhere.

We study the asymptotic distribution of the kinetic energy of the electrons as a function of their initial position over the transverse section of pulsed beams with OAM, both for a wide beam of $w_0 = 100.0$ μm and for a narrow beam of $w_0 = 6.4$ μm. The relative importance of the transverse structure effects and the role of longitudinal fields are addressed. We find that including the full paraxial fields with their longitudinal components, the asymptotic distribution of kinetic energy of an electron population distributed across the laser beam section, has a nontrivial rotational symmetry along the optical propagation axis. If we set $E_z = 0$, $B_z = 0$ in the numerical codes, the mentioned symmetry is broken to a lower one.

Position and velocity have been used in this work (Section 3.1 and Figures 3, 8, 11, 14 and 15) as dynamical variables to characterize the electron behavior; in other more theoretical studies, position and momentum are commonly used (Sections 3.1 and 4, Appendix A). In some of our most recent computations, and taking advantage of the identification of the scalar and vector potentials for paraxial fields, the Hamiltonian approach is used. Further results of this approach, under investigation but not included here, are fully compatible with those presented in the paper, and the computer algebra system Mathematica seems to deal with both descriptions of the dynamics in an efficient way.

A novel approach to corrections to the paraxial approximation is summarized in Appendix B. The exact solution X_{ex} of Equation (6), associated to Equation (5), is shown to fulfill a linear integral equation. The latter contains the paraxial function X_{par} (displaying a Gaussian structure) given in Equation (14) as the inhomogeneous term, a suitable Green function and $-\frac{\partial^2}{\partial z^2}$ (discarded in the framework of the paraxial approximation) as perturbation. The successive iterations of the integral equation give rise to corrections to X_{par}. One result of the analysis is that any iteration displays the same Gaussian structure as X_{par}.

Author Contributions: Conceptualization, I.P., R.F.Á.-E. and L.R.; methodology, I.P., R.F.Á.-E., L.R. and F.C.; software, I.P.; validation, I.P., R.F.Á.-E. and L.R.; formal analysis, R.F.Á.-E. and L.R.; investigation, I.P., R.F.Á.-E., L.R. and F.C.; writing—original draft preparation, I.P., R.F.Á.-E., L.R. and F.C.; writing—review and editing, I.P. All authors have read and agreed to the published version of the manuscript.

Funding: This research received no external funding.

Institutional Review Board Statement: Not applicable.

Informed Consent Statement: Not applicable.

Data Availability Statement: Numerical data supporting this research can be obtained from the corresponding author upon reasonable request.

Acknowledgments: I. P. acknowledges support from Ministerio de Ciencia, Innovación y Universidades (Spain) under Projects RTI2018-100835-B-I00 (MCIU/AEI/FEDER, UE) and RTI2018-096967-B-I00. R.F.A.-E. acknowledges support from Ministerio de Ciencia, Innovación y Universidades (Spain) under Project PGC2018-094684-B-C21 (contract partially funded by FEDER). L.R. acknowledges support from Laserlab V (Grant Agreement No. 871124, European Union Horizon 2020 INFRAIA research and innovation program), from IMPULSE (Grant Agreement No. 871161, European Union Horizon 2020 INFRADEV research and innovation program), and from Junta de Castilla y León Grant No. CLP087U16. R.F.A.-E. and F.C. are associate members of Instituto de Biocomputación y Física de los Sistemas Complejos, Universidad de Zaragoza, Zaragoza, Spain.

Conflicts of Interest: The authors declare no conflict of interest.

Appendix A. Analytical Solution of Electron Dynamics for a Transverse Pulsed Plane Wave

An analytical solution for the dynamics of an electron subject to a general transverse plane wave has been presented, in particular, in [27–32]. Based on them and by following the same approach as in [22], an analytical solution is presented below for the case of a purely transverse ($A_z \equiv 0$) pulsed vector potential depending solely on the variable $\zeta = \omega_0 t - k_0 z$. Notice that neither the Lorentz gauge nor the Lorentz condition are used here. Moreover, we set $\Phi = 0$.

Let us introduce dimensionless variables for the components of the vector potential according to:

$$\tilde{A}_x(\zeta) = qA_x(\zeta)/mc = 2\alpha_{A0}(\pi_0 \cos(\zeta - \phi_0) + \pi_1 \sin(\zeta - \phi_0))e^{-(\frac{\zeta-\eta_0}{\Delta})^2} \quad \text{(A1)}$$

$$\tilde{A}_y(\zeta) = qA_y(\zeta)/mc = 2\alpha_{A0}(\sigma_0 \cos(\zeta - \phi_0) + \sigma_1 \sin(\zeta - \phi_0))e^{-(\frac{\zeta-\eta_0}{\Delta})^2} \quad \text{(A2)}$$

where α_{A0} gives the amplitude of the field, $\Delta = \omega_0 \times T_p$ is a dimensionless parameter defining the temporal pulse width, η_0 is also dimensionless and defines the position at which the gaussian pulse is centered at $t = 0$, and ϕ_0 is the initial phase of the field. The real parameters $\pi_0, \pi_1, \sigma_0, \sigma_1$ fulfill $\pi_0^2 + \pi_1^2 + \sigma_0^2 + \sigma_1^2 = 1$, and describe the polarization state of the field.

The dimensionless coordinates and components of the (relativistic) momentum will be introduced according to

$$\tilde{x}(\zeta) = k_0 x(\zeta) \tag{A3}$$
$$\tilde{y}(\zeta) = k_0 y(\zeta) \tag{A4}$$
$$\tilde{z}(\zeta) = k_0 z(\zeta) \tag{A5}$$
$$\tilde{p}_x(\zeta) = p_x(\zeta)/mc \tag{A6}$$
$$\tilde{p}_y(\zeta) = p_y(\zeta)/mc \tag{A7}$$
$$\tilde{p}_z(\zeta) = p_z(\zeta)/mc \tag{A8}$$

One finds the general solution for the dynamics of the electron, through the general procedure indicated in [27] (see also [32]). By performing the corresponding integrals with the computer algebra system MATHEMATICA, one obtains for the momentum and position (as functions of ζ and/or the auxiliary variable(s) $\xi = \frac{\Delta^2+2i(\zeta-\eta_0)}{2\Delta}$, $\xi_0 = \frac{\Delta^2+2i(\zeta_0-\eta_0)}{2\Delta}$) the following expressions:

$$\tilde{p}_x(\zeta) = \tilde{f}_1 - \tilde{A}_x(\zeta) \tag{A9}$$
$$\tilde{p}_y(\zeta) = \tilde{f}_2 - \tilde{A}_y(\zeta) \tag{A10}$$
$$\tilde{p}_z(\zeta) = \frac{1-\tilde{\gamma}_1^2 + (\tilde{f}_1 - \tilde{A}_x(\zeta))^2 + (\tilde{f}_2 - \tilde{A}_y(\zeta))^2}{2\tilde{\gamma}_1} \tag{A11}$$
$$\tilde{x}(\zeta) = \frac{(\zeta-\zeta_0)\tilde{f}_1}{\tilde{\gamma}_1} - \frac{\alpha_{A0}\sqrt{\pi}\Delta}{\tilde{\gamma}_1} e^{-\frac{\Delta^2}{4}}\, \mathrm{Im}\left[e^{i(\eta_0-\phi_0)}(\pi_0 - i\pi_1)(\mathrm{Erfi}[\xi] - \mathrm{Erfi}[\xi_0])\right] \tag{A12}$$
$$\tilde{y}(\zeta) = \frac{(\zeta-\zeta_0)\tilde{f}_2}{\tilde{\gamma}_1} - \frac{\alpha_{A0}\sqrt{\pi}\Delta}{\tilde{\gamma}_1} e^{-\frac{\Delta^2}{4}}\, \mathrm{Im}\left[e^{i(\eta_0-\phi_0)}(\sigma_0 - i\sigma_1)(\mathrm{Erfi}[\xi] - \mathrm{Erfi}[\xi_0])\right] \tag{A13}$$
$$\tilde{z}(\zeta) = s_n(\zeta-\zeta_0) + \tilde{T}_{1z}(\zeta) + \tilde{T}_{2z}(\zeta) \tag{A14}$$

$$\tilde{T}_{1z}(\zeta) = -\frac{\alpha_{A0}\sqrt{\pi}\Delta e^{-\frac{\Delta^2}{4}}}{\tilde{\gamma}_1^2} \times \mathrm{Im}\left[e^{i(\eta_0-\phi_0)}((\pi_0 - i\pi_1)\tilde{f}_1 + (\sigma_0 - i\sigma_1)\tilde{f}_2)(\mathrm{Erfi}[\xi] - \mathrm{Erfi}[\xi_0])\right] \tag{A15}$$

$$\tilde{T}_{2z}(\zeta) = \frac{\alpha_{A0}^2}{2\tilde{\gamma}_1^2}\sqrt{\frac{\pi}{2}}\Delta e^{-\frac{\Delta^2}{2}}\left\{e^{\frac{\Delta^2}{2}}\left(\mathrm{Erf}(\frac{\sqrt{2}(\zeta-\eta_0)}{\Delta}) - \mathrm{Erf}(\frac{\sqrt{2}(\zeta_0-\eta_0)}{\Delta})\right) + \right.$$
$$\left. + \mathrm{Im}\left[e^{2i(\eta_0-\phi_0)}[\pi_0^2 - \pi_1^2 + \sigma_0^2 - \sigma_1^2 - 2i(\pi_0\pi_1 + \sigma_0\sigma_1)](\mathrm{Erfi}(\sqrt{2}\xi) - \mathrm{Erfi}(\sqrt{2}\xi_0))\right\} \tag{A16}$$

To complete the solution of the dynamical problem, expressions should be provided for trajectory time and time at detector as a function of ζ: see the corresponding formulas below. With all this information, a full description of the dynamics in parametric form is obtained, as well as an efficient computation of the temporal evolution of the radiated E and B at the detector, via the Lienard-Wiechert expressions for the fields, and the connection between ζ and τ [22,32]. In what follows n_1, n_2, n_3 are the components of the unit scattering vector directed from the origin of coordinates to the point at which the scattered radiation is computed. They should fulfill $n_1^2 + n_2^2 + n_3^2 = 1$.

$$\tau' - \tau_0' =$$
$$\frac{(1+\tilde{f}_1^2+\tilde{f}_2^2+\tilde{\gamma}_1^2)(\zeta-\zeta_0)}{2\tilde{\gamma}_1^2} + \frac{\sqrt{\frac{\pi}{2}}\Delta\alpha_{A0}^2}{2\tilde{\gamma}_1^2}\left(\mathrm{erf}\left[\frac{\sqrt{2}(\zeta-\eta_0)}{\Delta}\right] - \mathrm{erf}\left[\frac{\sqrt{2}(\zeta_0-\eta_0)}{\Delta}\right]\right) -$$
$$\sqrt{\frac{\pi}{2}}\frac{\Delta\alpha_{A0}^2}{4\tilde{\gamma}_1^2}e^{-\frac{\Delta^2}{2}}\,\mathrm{Im}\left[e^{-2i(\eta_0-\phi_0)}(\pi_0^2 + 2i\pi_0\pi_1 - \pi_1^2 + (\sigma_0 + i\sigma_1)^2)\left(\mathrm{Erfi}\left[\sqrt{2}\xi^*\right] - \mathrm{Erfi}\left[\sqrt{2}(\xi_0)^*\right]\right)\right] +$$
$$\mathrm{Re}\left[\frac{e^{-\frac{\Delta^2}{4}}\sqrt{\pi}\Delta\alpha_{A0}}{2\tilde{\gamma}_1^2}e^{i(\eta_0-\phi_0)}((i\pi_0 + \pi_1)\tilde{f}_1 + (i\sigma_0 + \sigma_1)\tilde{f}_2)(\mathrm{Erfi}[\xi] - \mathrm{Erfi}[\xi_0]) + \right.$$
$$\frac{\sqrt{\pi}\Delta\alpha_{A0}}{8\tilde{\gamma}_1^2}e^{-\frac{\Delta^2}{2}-i(\eta_0+2\phi_0)}\left(-i\sqrt{2}e^{3i\eta_0}\mathrm{Erfi}\left[\sqrt{2}\xi\right]\alpha_{A0}(\pi_0^2 - 2i\pi_0\pi_1 - \pi_1^2 + (\sigma_0 - i\sigma_1)^2) + \right.$$
$$i\sqrt{2}e^{3i\eta_0}\mathrm{Erfi}\left[\sqrt{2}\xi_0\right]\alpha_{A0}(\pi_0^2 - 2i\pi_0\pi_1 - \pi_1^2 + (\sigma_0 - i\sigma_1)^2) +$$
$$\left.\left. 4e^{\frac{\Delta^2}{4}+3i\phi_0}(\mathrm{Erfi}[\xi^*] - \mathrm{Erfi}[(\xi_0)^*])((-i\pi_0 + \pi_1)\tilde{f}_1 + (-i\sigma_0 + \sigma_1)\tilde{f}_2)\right)\right]$$

$$
\begin{aligned}
&\tau-\tau_0=\\
&\frac{1}{8}\Bigg(\sqrt{2\pi}\mathrm{Im}\left[\frac{e^{-\frac{\Delta^2}{2}-2i\eta_0+2i\phi_0}(-1+\mathrm{n3})\Delta\mathrm{Erfi}\left[\sqrt{2}\tilde{\xi}^*\right]\alpha_{\mathrm{A0}}^2\left((\pi_0+i\pi_1)^2+\sigma_0^2+2i\sigma_0\sigma_1-\sigma_1^2\right)}{\tilde{\gamma}_1^2}\right]-\\
&\sqrt{2\pi}\mathrm{Im}\left[\frac{e^{-\frac{\Delta^2}{2}-2i\eta_0+2i\phi_0}(-1+\mathrm{n3})\Delta\mathrm{Erfi}\left[\sqrt{2}(\xi_0)^*\right]\alpha_{\mathrm{A0}}^2\left((\pi_0+i\pi_1)^2+\sigma_0^2+2i\sigma_0\sigma_1-\sigma_1^2\right)}{\tilde{\gamma}_1^2}\right]+\\
&\mathrm{Re}\left[\frac{1}{\tilde{\gamma}_1^2}\left(-2(-1+\mathrm{n3})\sqrt{2\pi}\Delta\left(\mathrm{Erf}\left[\frac{\sqrt{2}(\zeta-\eta_0)}{\Delta}\right]-\mathrm{Erf}\left[\frac{\sqrt{2}(\zeta_0-\eta_0)}{\Delta}\right]\right)\alpha_{\mathrm{A0}}^2+\right.\right.\\
&e^{-\frac{\Delta^2}{2}-i\eta_0-2i\phi_0}\sqrt{\pi}\Delta\alpha_{\mathrm{A0}}\Big(i\sqrt{2}e^{3i\eta_0}(-1+\mathrm{n3})\mathrm{Erfi}\left[\sqrt{2}\tilde{\xi}\right](\pi_0-i\pi_1)^2\alpha_{\mathrm{A0}}-\\
&i\sqrt{2}e^{3i\eta_0}(-1+\mathrm{n3})\mathrm{Erfi}\left[\sqrt{2}\xi_0\right](\pi_0-i\pi_1)^2\alpha_{\mathrm{A0}}+\\
&i\sqrt{2}e^{3i\eta_0}(-1+\mathrm{n3})\mathrm{Erfi}\left[\sqrt{2}\tilde{\xi}\right]\alpha_{\mathrm{A0}}(\sigma_0-i\sigma_1)^2-\\
&i\sqrt{2}e^{3i\eta_0}(-1+\mathrm{n3})\mathrm{Erfi}\left[\sqrt{2}\xi_0\right]\alpha_{\mathrm{A0}}(\sigma_0-i\sigma_1)^2+\\
&4ie^{\frac{\Delta^2}{4}+3i\phi_0}(-1+\mathrm{n3})\mathrm{Erfi}[\xi^*](\pi_0+i\pi_1)\tilde{f}_1+\\
&4e^{\frac{\Delta^2}{4}+3i\phi_0}(-1+\mathrm{n3})\mathrm{Erfi}[(\xi_0)^*](-i\pi_0+\pi_1)\tilde{f}_1+\\
&4ie^{\frac{\Delta^2}{4}+3i\phi_0}(-1+\mathrm{n3})\mathrm{Erfi}[\xi^*](\sigma_0+i\sigma_1)\tilde{f}_2+\\
&4e^{\frac{\Delta^2}{4}+3i\phi_0}(-1+\mathrm{n3})\mathrm{Erfi}[(\xi_0)^*](-i\sigma_0+\sigma_1)\tilde{f}_2+\\
&4ie^{\frac{\Delta^2}{4}+3i\phi_0}\mathrm{n1}(\mathrm{Erfi}[\xi^*]-\mathrm{Erfi}[(\xi_0)^*])(\pi_0+i\pi_1)\tilde{\gamma}_1+\\
&\left.4ie^{\frac{\Delta^2}{4}+3i\phi_0}\mathrm{n2}(\mathrm{Erfi}[\xi^*]-\mathrm{Erfi}[(\xi_0)^*])(\sigma_0+i\sigma_1)\tilde{\gamma}_1\Big)-\right.\\
&4(\zeta-\zeta_0)\left(-1+\mathrm{n3}+(-1+\mathrm{n3})\tilde{f}_1^2+(-1+\mathrm{n3})\tilde{f}_2^2+2\mathrm{n1}\tilde{f}_1\tilde{\gamma}_1+2\mathrm{n2}\tilde{f}_2\tilde{\gamma}_1-\tilde{\gamma}_1^2-\mathrm{n3}\tilde{\gamma}_1^2\right)+\\
&4e^{-\frac{\Delta^2}{4}+i\eta_0-i\phi_0}\sqrt{\pi}\Delta\mathrm{Erfi}[\tilde{\xi}]\alpha_{\mathrm{A0}}\\
&\left(-i(-1+\mathrm{n3})(\pi_0-i\pi_1)\tilde{f}_1+\mathrm{n1}(-i\pi_0-\pi_1)\tilde{\gamma}_1-i(\sigma_0-i\sigma_1)\left((-1+\mathrm{n3})\tilde{f}_2+\mathrm{n2}\tilde{\gamma}_1\right)\right)+\\
&4e^{-\frac{\Delta^2}{4}+i\eta_0-i\phi_0}\sqrt{\pi}\Delta\mathrm{Erfi}[\tilde{\xi}_0]\alpha_{\mathrm{A0}}\\
&\left.\left.\left((-1+\mathrm{n3})(i\pi_0+\pi_1)\tilde{f}_1+\mathrm{n1}(i\pi_0+\pi_1)\tilde{\gamma}_1+(i\sigma_0+\sigma_1)\left((-1+\mathrm{n3})\tilde{f}_2+\mathrm{n2}\tilde{\gamma}_1\right)\right)\right)\right]\Bigg)
\end{aligned}
$$

Notice that ξ, ξ_0 are complex numbers in general , while $\zeta, \zeta_0, \eta_0, \phi_0$ are real numbers. $\mathrm{Erfi}(z)$ is defined for a general complex argument z as

$$\mathrm{Erfi}(z) \equiv -i \times \mathrm{erf}(iz) \tag{A17}$$

and

$$\mathrm{erf}(z) = \mathrm{Erf}(z) = \frac{2}{\sqrt{\pi}}\int_0^z e^{-t^2}dt \tag{A18}$$

Appendix B. Corrections to the Paraxial Approximation

Corrections to the paraxial approximation, going beyond the former, will be studied here (through a new approach, to the best of the authors knowledge). Specifically, how the exact solution X_{ex} of Equation (6), associated to Equation (5), differs from the solution X_{par} of Equation (14) will be analyzed. For that purpose, $-\frac{\partial^2}{\partial z^2}$ will be treated as a perturbation and, so, Equation (6) will be recast as:

$$(\nabla_{\bar{x}}^2 + 2ik_0\frac{\partial}{\partial z})X_{ex} = -\frac{\partial^2}{\partial z^2}X_{ex} \tag{A19}$$

Equation (A19) will be transformed into an integral equation which will enable to analyze the corrections to X_{par}. For that purpose, a Green function $G_{par} = G_{par}(\bar{x}-\bar{x}_1, z-z_1)$ of Equation (14) (to be referred to as paraxial Green function) will be introduced. It fulfills:

$$(\nabla_{\bar{x}}^2 + 2ik_0\frac{\partial}{\partial z})G_{par}(\bar{x}-\bar{x}_1, z-z_1) = \delta^2(\bar{x}-\bar{x}_1)\delta(z-z_1) \tag{A20}$$

where δ and δ^2 denote the one- and two-dimensional Dirac delta functions. $G_{par}(\bar{x}-\bar{x}_1, z-z_1)$ is defined so as to imply propagation towards increasing z (say, for $z-z_1>0$), in agreement with the similar propagation ($\exp i(k_0 z-\omega_0 t)$) in Equation (5). Upon Fourier transforming the last equation, one finds through a standard calculation:

$$G_{par}(\bar{x}-\bar{x}_1, z-z_1)=\int \frac{d^2\bar{l}dl_z}{(2\pi)^3}\frac{\exp i[\bar{l}(\bar{x}-\bar{x}_1)+l_z(z-z_1)]}{-\bar{l}^2-2k_0 l_z+i\epsilon} \tag{A21}$$

with $\epsilon>0$, very small and $\to 0$ at the end of the computation. The inclusion of $i\epsilon$ enables to implement propagation towards increasing $z-z_1>0$. Upon performing a residue integration in the complex l_z-plane and a Gaussian integration over $\bar{l}$, one obtains:

$$G_{par}(\bar{x}-\bar{x}_1, z-z_1)=-\frac{\theta(z-z_1)}{4\pi(z-z_1)}\exp i[\frac{k_0(\bar{x}-\bar{x}_1)^2}{2(z-z_1)}] \tag{A22}$$

$\theta(z-z_1)$ being the step function. The integral equation yielding the full solution X_{ex} of Equation (6) and, so, the corrections to $X_{par}=g_{0,0}(\bar{x},z)$ (Equation (14)) reads:

$$X_{ex}(\bar{x},z)=g_{0,0}(\bar{x},z)+\int d^2\bar{x}_1\int dz_1 G_{par}(\bar{x}-\bar{x}_1,z-z_1)\times$$
$$[-\frac{\partial^2}{\partial z_1^2}X_{ex}(\bar{x}_1,z_1)] \tag{A23}$$

$g_{0,0}(\bar{x},z)$ is given in Equation (21). The right-hand side of the last equation is easily seen to satisfy Equation (A19). Equation (A23), by indefinite successive iterations, yields $X_{ex}(\bar{x},z)$ as the following infinite series solving Equation (A19):

$$X_{ex}(\bar{x},z)=g_{0,0}(\bar{x},z)+\sum_{m=1}^{+\infty} g_{0,0}(\bar{x},z)^{(m)} \tag{A24}$$
$$g_{0,0}(\bar{x},z)^{(m+1)}=\int d^2\bar{x}_1\int dz_1 G_{par}(\bar{x}-\bar{x}_1,z-z_1)\times$$
$$[-\frac{\partial^2}{\partial z_1^2}g_{0,0}(\bar{x}_1,z_1)^{(m)}, m=0,1,2,... \tag{A25}$$

The integration over $\bar{x}_1$ in $g_{0,0}(\bar{x},z)^{(m+1)}$ when use is made of Equation (21) and $G_{par}(\bar{x}-\bar{x}_1, z-z_1)$, is Gaussian, to all orders in m. By performing it, the following important property follows for $m=1,2,3...$

$$g_{0,0}(\bar{x},z)^{(m)}=(2/\pi)^{1/2}\exp[-\frac{\rho^2}{w(z)^2}]\exp[i\frac{z}{z_0}\frac{\rho^2}{w(z)^2}]f_{0,0}(\frac{\rho^2}{z_0^2},\frac{z}{z_0},\epsilon_0)^{(m)} \tag{A26}$$

where $f_{0,0}(\frac{\rho^2}{z_0^2},\frac{z}{z_0},\epsilon_0)^{(m)}$ is a polynomial of degree $2m$ in $\frac{\rho^2}{z_0^2}$. That is, the Gaussian structures $\exp[-\frac{\rho^2}{w(z)^2}]\exp[i\frac{z}{z_0}\frac{\rho^2}{w(z)^2}]$ in $g_{0,0}(\bar{x},z)$ reproduce themselves to all orders of iteration. Then:

$$X_{ex}(\bar{x},z)=\exp[-\frac{\rho^2}{w(z)^2}]\exp[i\frac{z}{z_0}\frac{\rho^2}{w(z)^2}]\times$$
$$[f_{0,0}(\frac{z}{z_0})+\sum_{m=1}^{+\infty} f_{0,0}(\frac{\rho^2}{z_0^2},\frac{z}{z_0},\epsilon_0)^{(m)}] \tag{A27}$$

The first iteration is:

$$f_{0,0}(\frac{\rho^2}{z_0^2}, \frac{z}{z_0}, \epsilon_0)^{(1)} = -\int dz_2 \frac{\theta(z/z_0 - z_2)}{4\pi(z/z_0 - z_2)} C(z/z_0, z_2; \frac{\rho^2}{w(z)^2}, \epsilon_0)^{(1)} \quad \text{(A28)}$$

$$C(z/z_0, z_2; \frac{\rho^2}{w(z)^2}, \epsilon_0)^{(1)} = \sum_{n=0}^{2} C_{2n}(z/z_0, z_2; \epsilon_0)^{(1)} [\frac{\rho^2}{w(z)^2}]^n \quad \text{(A29)}$$

$$C_0(z/z_0, z_2; \epsilon_0)^{(1)} = \epsilon_0^2[-\frac{\pi}{A}\frac{\partial^2 f_{0,0}(z/z_0)}{\partial z_2^2} + [2\frac{\partial f_{0,0}(z/z_0)}{\partial z_2}\frac{\partial}{\partial z_2}\frac{1}{1+iz_2} + f_{0,0}(z/z_0)\frac{\partial^2}{\partial z_2^2}\frac{1}{1+iz_2}]\frac{\pi}{A^2} - f_{0,0}(z/z_0)(\frac{\partial}{\partial z_2}\frac{1}{1+iz_2})^2\frac{2\pi}{A^3}] \quad \text{(A30)}$$

$$C_2(z/z_0, z_2; \epsilon_0)^{(1)} = [2\frac{\partial f_{0,0}(z/z_0)}{\partial z_2}\frac{\partial}{\partial z_2}\frac{1}{1+iz_2} + f_{0,0}(z/z_0)\frac{\partial^2}{\partial z_2^2}\frac{1}{1+iz_2}]\frac{\pi}{A^3}(\frac{1}{(z/z_0 - z_2)^2} - f_{0,0}(z/z_0)(\frac{\partial}{\partial z_2}\frac{1}{1+iz_2})^2\frac{4\pi}{A^4}\frac{1}{(z/z_0 - z_2)^2} \quad \text{(A31)}$$

$$C_4(z/z_0, z_2; \epsilon_0)^{(1)} = \epsilon_0^{-2} f_{0,0}(z/z_0)(\frac{\partial}{\partial z_2}\frac{1}{1+iz_2})^2\frac{1}{(z/z_0 - z_2)^4}\frac{\pi}{A^5} \quad \text{(A32)}$$

$$A = \frac{i - (z/z_0)}{(z/z_0 - z_2)(1+iz_2)} \quad \text{(A33)}$$

Let a finite number, M, be kept in the series yielding $X_{ex}(\bar{x}, z)$ and let the resulting finite sum be rewritten as:

$$X_{ex}(\bar{x}, z) = \exp[-\frac{\rho^2}{\epsilon_0^2 z_0^2}]\frac{1 - i(z/z_0)}{1 + (z/z_0)^2}\frac{\rho^2}{w(z)^2}] \times [f_{0,0}(\frac{z}{z_0}) + \sum_{m=1}^{+M} f_{0,0}(\frac{\rho^2}{z_0^2}, \frac{z}{z_0}, \epsilon_0)^{(m)}] \quad \text{(A34)}$$

As $\epsilon_0 \to 0$, for fixed z_0, the right-hand-side of the last finite sum in Equation (A34) approaches zero. It is open whether the full series giving $X_{ex}(\bar{x}, z)$ is an asymptotic one.

References

1. Danson, C.N.; Haefner, C.; Bromage, J.; Butcher, T.; Chanteloup, J.-C.F.; Chowdhury, E.A.; Galvanauskas, A.; Gizzi, L.A.; Hein, J.; Hillier, D.I.; et al. Petawatt and exawatt class lasers worldwide. *High Power Laser Sci. Eng.* **2019**, *7*, e54. [CrossRef]
2. Yoon, J.W.; Kim, Y.G.; Choi, I.W.; Sung, J.H.; Lee, H.W.; Lee, S.K.; Nam, C.H. Realization of laser intensity over 10^{23} W/cm^2, *Optica* **2021**, *8*, 630 [CrossRef]
3. Rohrlich, F. *Classical Charged Particles*, 3rd ed.; World Scientific: Singapore, 2007.
4. Froula, D.H.; Glenzer, S.H.; Luhmann, N.C., Jr.; Sheffield, J. *Plasma Scattering of Electromagnetic Radiation: Theory and Measurement Techniques*; Academic Press, Elsevier: Amsterdam, The Netherlands, 2011.
5. Hutchison, I. *Principles of Plasma Diagnostics*; Cambridge University Press: Cambridge, UK, 2006.
6. Allen , L.; Barnett , S.M.; Padgett, M.J. *Optical Angular Momentum*; IOP Publishing: London, UK, 2003.
7. Torres, J.P.; Torner, L. (Eds) *Twisted Photons: Applications of Light with Orbital Angular Momentum*; Wiley-VCH: Weinheim, Germany, 2011.
8. Simon D.S, A Guided Tour to Light Beams: From Lasers to Optical Knots; *IoPConcise Physics*, Bristol, UK, 2016.
9. Calvo, G.F.; Picon, A.; Bagan, E. Quantum field theory of photons with orbital angular momentum, *Phys. Rev. A*. **2006** *73*, 013805. [CrossRef]

10. Karimi, E.; Schulz, S.A.; De Leon, I.; Qassim, H.; Upham. J.; Boyd, R.W. Generating optical orbital angular momentum at visible wavelengths using a plasmonic metasurface *Nat. Commun. Light Sci. Appl.* **2014**, *3*, e167. [CrossRef]
11. Noyan, M.A.; Kikkawa, J.M. Time-resolved orbital angular momentum spectroscopy. *Appl. Phys. Lett.* **2015**, *107*, 032406. [CrossRef]
12. Persuy, D.; Ziegler, M.; Crégut. O.; Kheng. K.; Gallart. M,; Hönerlage, B.; Gilliot, P. Four-wave mixing in quantum wells using femtosecond pulses with Laguerre-Gauss modes. *Phys. Rev.* **2015**, *B92*, 115312. [CrossRef]
13. Schmiegelow, C.T.; Schulz. J.; Kaufmann. H.; Ruster, T.; Poschinger, U.G.; Schmidt-Kaler, F. Transfer of optical orbital angular momentum to a bound electron. *Nat. Commun.* **2018**, *7*, 12998. [CrossRef] [PubMed]
14. Seghilani, M.S.; Myara, M.; Sellahi , M.; Legratiet, L.; Sagnes, I.; Beaudoin, G.; Lalanne, P.; Garnache, A. Vortex Laser based on III-V semiconductor metasurface: direct generation of coherent Laguerre-Gauss modes carrying controlled orbital angular momentum. *Sci. Rep.* **2016**, *6*, 38156. [CrossRef]
15. Shigematsu, K.; Yamane, K.; Morita, R.; Toda, Y. Coherent dynamics of exciton orbital angular momentum transferred by optical vortex pulses. *Phys. Rev.* **2016**, *B93*, 045205. [CrossRef]
16. Picon, A.; Benseny, A.; Mompart, J.; Vazquez de Aldana, J.R.; Plaja, L.; Calvo, G.F.; Roso, L. Transferring orbital and spin angular momenta of light to atoms. *New J. Phys.* **2010**, *12, 083053* . [CrossRef]
17. Longman, A.; Salgado, C.; Zeraouli, G.H.; Apiñaniz, J.I.; Perez-Hernandez, J.A.; Eltahlawy, M.K.; Volpe, L.; Fedosejevs, R. Off-axis spiral phase mirrors for generating high-intensity optical vortices. *Opt. Lett.* **2020**, *45* 2187 [CrossRef] [PubMed]
18. Erikson, W.L.; Singh, S. Polarization properties of Maxwell-Gaussian laser beams.*Phys. Rev. E* **1994** *49*, 5778–5786. [CrossRef]
19. Peatross, J.; Berrondo, M.; Smith, D.; Ware, M.Vector fields in a tight laser focus: comparison of models. *Opt. Express* **2017**, *25*, 13990–14007. [CrossRef] [PubMed]
20. Ghebregziabher, I.; Shadwick, B.A.; Umstadter, D. Spectral bandwidth reduction of Thomson scattered light by pulse chirping. *Phys. Rev. Accel. Beams* **2013**, *16*, 030705. [CrossRef]
21. Pastor, I.; Alvarez-Estrada, R.F.; Roso, L.; Castejon, F.; Guasp, J. Nonlinear relativistic electron Thomson scattering for laserradiation with orbital angular momentum. *J. Phys. Commun.* **2020**, *4*, 065010. [CrossRef]
22. Pastor, I.; Alvarez-Estrada, R.F.; Roso, L.; Guasp, J; Castejon, F. Electron Dynamics and Thomson Scattering for Ultra-Intense Lasers: Elliptically Polarized and OAM Beams. *Photonics* **2021**, *8*, 182. [CrossRef]
23. Panofsky, W.K.; Phillips, M. Classical Electricity and Magnetism. *Addison-Wesley*, USA, 1962.
24. Roso, L.; Pérez-Hernández, J.A.; Lera, R.; Fedosejevs, R. The Role of the Ponderomotive Force in High Field Experiments. In *Progress in Ultrafast intense Laser Science XVI*; Yamanouchi, K., Midorikawa, K., Roso, L., Eds.; Springer: Cham, Switzerland, 2021; p. 149.
25. Moore, C.I. Confinement of electrons to the centre of a laser focus via the ponderomotive potential. *J. Mod. Opt.* **1992**, *39* 2171. [CrossRef]
26. Shao, B.; Li, Y.; Peng, Y.; Wang, P.; Qian, J.; Leng, Y.; Li, R. Broad-bandwidth high-temporal-contrast carrier-envelope-phase-stabilized laser seed for 100 PW lasers. *Opt. Lett.* **2020**, *45*, 2215. [CrossRef]
27. Landau, L.D.; Lifchitz, E.M. *The Classical Theory of Fields*, 4th ed.; Pergamon Press: New York, NY, USA, 1975.
28. Sarachik, E.S.; Schappert, G.T. Classical theory of the scattering of intense laser radiation by free electrons. *Phys. Rev. D* **1970**, *1*, 2738. [CrossRef]
29. Essarey, E.; Ride, S.K.; Sprangle, P. Nonlinear Thomson scattering of intense laser pulses from beams and plasmas. *Phys. Rev. E* **1993**, *48*, 3003. [CrossRef]
30. Ride, S.K.; Essarey, E.; Baine, M. Thomson scattering of intense lasers from electron beams at arbitrary interaction angles. *Phys. Rev. E* **1995**, *52*, 5425. [CrossRef] [PubMed]
31. Avetissian, H. *Relativistic Nonlinear Electrodynamics*; Springer Series in Optical Sciences; Springer: New York, NY, USA, 2006.
32. Alvarez-Estrada, R.F.; Pastor, I.; Guasp, J.; Castejon, F. Nonlinear relativistic single-electron Thomson scattering power spectrum for incoming laser of arbitrary intensity. *Phys. Plasmas* **2012**, *19*, 062302.